# Internal Variability in Projections of Twenty-First-Century Arctic Sea Ice Loss: Role of the Large-Scale Atmospheric Circulation

JUSTIN J. WETTSTEIN AND CLARA DESER

*National Center for Atmospheric Research,* Boulder, Colorado*

(Manuscript received 27 November 2012, in final form 7 June 2013)

ABSTRACT

Internal variability in twenty-first-century summer Arctic sea ice loss and its relationship to the large-scale atmospheric circulation is investigated in a 39-member Community Climate System Model, version 3 (CCSM3) ensemble for the period 2000–61. Each member is subject to an identical greenhouse gas emissions scenario and differs only in the atmospheric model component's initial condition.

September Arctic sea ice extent trends during 2020–59 range from $-2.0 \times 10^6$ to $-5.7 \times 10^6$ km$^2$ across the 39 ensemble members, indicating a substantial role for internal variability in future Arctic sea ice loss projections. A similar nearly threefold range (from $-7.0 \times 10^3$ to $-19 \times 10^3$ km$^3$) is found for summer sea ice volume trends.

Higher rates of summer Arctic sea ice loss in CCSM3 are associated with enhanced transpolar drift and Fram Strait ice export driven by surface wind and sea level pressure patterns. Over the Arctic, the covarying atmospheric circulation patterns resemble the so-called Arctic dipole, with maximum amplitude between April and July. Outside the Arctic, an atmospheric Rossby wave train over the Pacific sector is associated with internal ice loss variability. Interannual covariability patterns between sea ice and atmospheric circulation are similar to those based on trends, suggesting that similar processes govern internal variability over a broad range of time scales. Interannual patterns of CCSM3 ice–atmosphere covariability compare well with those in nature and in the newer CCSM4 version of the model, lending confidence to the results. Atmospheric teleconnection patterns in CCSM3 suggest that the tropical Pacific modulates Arctic sea ice variability via the aforementioned Rossby wave train. Large ensembles with other coupled models are needed to corroborate these CCSM3-based findings.

## 1. Introduction

September Arctic sea ice extent has decreased by slightly more than $2.5 \times 10^6$ km$^2$ ($\sim$10% decade$^{-1}$) since 1979, when consistent satellite observations were initiated (Fetterer et al. 2002, with updates; Serreze et al. 2007; Comiso et al. 2008; Deser and Teng 2008). Comprehensive Arctic sea ice thickness measurements are more difficult to retrieve, but available measurements (Rothrock et al. 1999) and surrogate measures such as the fraction of multiyear ice (Nghiem et al. 2006) and ice age (Maslanik et al. 2007) indicate ice thickness and volume losses are also occurring. Most coupled climate models forced with increasing greenhouse gas (GHG) concentrations simulate reductions in Arctic summer sea ice over the late twentieth century, a trend that accelerates over the twenty-first century (Stroeve et al. 2007, 2012). Such models commonly forecast an essentially ice-free ($<1 \times 10^6$ km$^2$) summer Arctic by mid to late twenty-first century (e.g., Meehl et al. 2006; Stroeve et al. 2007; Kay et al. 2011; Meehl et al. 2012; Vavrus et al. 2012; Bitz et al. 2012; Stroeve et al. 2012). The magnitude and rate of projected twenty-first-century Arctic sea ice loss is subject to considerable uncertainty, however (Stroeve et al. 2007, 2012).

Uncertainty regarding the magnitude and rate of Arctic sea ice loss stems from 1) different assumptions regarding future external (GHG) forcing, 2) intermodel spread resulting from different model physics and parameterizations, and 3) internally generated variability (e.g., Tebaldi and Knutti 2007; Hawkins and Sutton 2009; Deser et al. 2012b). By comparing observations to simulated trends in a 6-member ensemble of the Community

*The National Center for Atmospheric Research is sponsored by the National Science Foundation.

*Corresponding author address:* Justin J. Wettstein, College of Earth, Ocean, and Atmospheric Sciences, School of Public Policy, Oregon State University, 104 CEOAS Administration Building, Corvallis, OR 97331.
E-mail: justinw@coas.oregonstate.edu

DOI: 10.1175/JCLI-D-12-00839.1

Climate System Model, version 4 (CCSM4), Kay et al. (2011) estimated that approximately half (56%) of the observed rate of 1979–2005 September Arctic sea ice extent decline was externally forced, with the remainder due to internal climate variability. A similar fraction (60%) of the observed 1979–2011 sea ice loss was attributed to external forcing by Stroeve et al. (2012) based on a comparison with the multimodel ensemble mean of simulations from phase 5 of the Climate Model Intercomparison Project (CMIP5).

The sensitivity of Arctic sea ice loss projections to the amount of external forcing was evaluated in CMIP3 and CMIP5 by subjecting each model to different levels of GHG increases. Significant differences in ice loss do not emerge until approximately the middle of the twenty-first century [e.g., Figs. 12 and 19, respectively, in Meehl et al. (2006, 2012)] when atmospheric GHG concentrations associated with the different GHG emissions scenarios begin to diverge substantially [e.g., Fig. 5 in Moss et al. (2010)].

The intermodel spread in projected Arctic summer sea ice decline is roughly comparable in magnitude to the multimodel-mean estimate of greenhouse gas–forced sea ice loss over at least the next several decades in the CMIP3 and CMIP5 archives [e.g., Figs. 1 and 2, respectively, in Stroeve et al. (2007, 2012)]. Intermodel spread in ice loss is often accompanied by differences in the intensity of local surface energy budget feedbacks (DeWeaver et al. 2008; Bitz 2008; Winton 2008; Boé et al. 2010; Kay et al. 2012), ocean heat transports (Holland and Bitz 2003; Mahlstein and Knutti 2011; Kay et al. 2012; Bitz et al. 2012), or atmospheric heat transports (Winton 2008). DeWeaver and Bitz (2006) found substantially different climatological-mean surface wind and ice advection patterns resulting in substantially different climatological-mean Arctic sea ice amounts and distributions in two multicentury control simulations of the Community Climate System Model, version 3 (CCSM3), when two different spatial resolutions were prescribed for the component Community Atmosphere Model, version 3 (CAM3). A strong model-dependent relationship is also evident between the amount of Arctic sea ice in the late twentieth century and the amount at the end of the twenty-first century in ensembles from both CMIP3 [e.g., Fig. 1 in Stroeve et al. (2007)] and CMIP5 [e.g., Fig. 2 in Stroeve et al. (2012)].

In contrast to the first two sources of uncertainty outlined above, the role of internal variability in twenty-first-century Arctic sea ice loss has received substantially less attention. Holland et al. (2008) noted that internal variability plays an important role in CCSM3 simulations of abrupt losses in September sea ice extent. Kay et al. (2011) and Jahn et al. (2012) described highly variable Arctic sea ice loss trends in a small (6-member) set of CCSM4 simulations of the late twentieth century. Kay et al. (2011) also noted that internal variability influences both the magnitude and sign of projected future Arctic sea ice trends well into the twenty-first century. The purpose of this study is to comprehensively evaluate the uncertainty in future Arctic sea ice loss associated with internally generated climate variability, using a single coupled climate model and a much larger (39-member) set of simulations than in previous studies. We also expand on earlier work by investigating the mechanisms that control future internally generated Arctic sea ice loss.

Observed interannual and decadal-scale variability in Arctic sea ice extent has been related to variability in atmospheric circulation patterns that can be characterized as either regional (Vinje 2001; Tsukernik et al. 2010) or hemispheric in scale (Rigor et al. 2002; Rigor and Wallace 2004; Belchansky et al. 2005; Overland and Wang 2005; Wu et al. 2006; Ogi and Wallace 2007; L'Heureux et al. 2008; Wang et al. 2009; Overland and Wang 2010; Ogi et al. 2010; Screen et al. 2011; Stroeve et al. 2011; Ogi and Wallace 2012). Smedsrud et al. (2011) linked changes in Fram Strait sea ice export to anomalous Arctic wind patterns and pan-Arctic sea ice variability. Observed sea ice variability has also been related to anomalies in the thermodynamic exchange of energy across the ice–ocean–atmosphere interface (Francis and Hunter 2007; Perovich et al. 2007) and to anomalies in ocean heat transport (Polyakov et al. 2005; Shimada et al. 2006). We note that changes in the surface energy budget and ocean heat transport may in turn be associated with variations in the atmospheric circulation. In the studies that relate ice loss to large-scale atmospheric variability, there are divergent views on the spatial structure and seasonality of the covariant circulation anomalies. Covariant central Arctic surface pressure patterns that resemble the Arctic Oscillation (AO; Thompson and Wallace 1998) are described by many studies (Rigor et al. 2002; Rigor and Wallace 2004; Belchansky et al. 2005; Ogi and Wallace 2007; Ogi et al. 2010; Stroeve et al. 2011; Ogi and Wallace 2012), whereas patterns more consistent with the dipole anomaly (Wu et al. 2006) and Arctic dipole (AD; Overland and Wang 2010) are identified in others (Overland and Wang 2005; Wu et al. 2006; Wang et al. 2009; Overland and Wang 2010; Screen et al. 2011). L'Heureux et al. (2008) noted an unusually strong midtropospheric anticyclone over the western Arctic and a Pacific/North American (PNA)-like pattern extending into the midlatitudes during the months preceding the previous record low September sea ice extent in 2007. Even though the studies above preferentially cluster around either AO- or AD-like patterns

over the central Arctic, individual studies within each group diverge substantially on the seasonality of the ice–atmosphere relationships identified.

In this study, we investigate uncertainty in Arctic sea ice loss projections over the coming decades due to internal variability in the climate system, with a particular focus on the role of the atmospheric circulation. We use a unique 39-member CCSM3 ensemble of climate change simulations for the 2000–61 period. This set of simulations has previously been used to assess climate predictability (Branstator and Teng 2010; Teng and Branstator 2011) and to compare anthropogenically forced and internally generated contributions to future climate change signals in temperature, precipitation, and atmospheric circulation (Deser et al. 2012a,b; Hu et al. 2012). We also make use of smaller twenty-first-century climate change simulation ensembles with the newer version of the model, CCSM4. In addition, we analyze the relatively short observational record to assess the realism of the physical relationships between Arctic sea ice and atmospheric circulation variability on interannual time scales as simulated by the models. The model simulations, observational datasets, and analysis methods are described in section 2. Results are presented in section 3 and summarized in section 4. A discussion concludes the paper.

## 2. Data and methods

The primary dataset used in this study is a unique ensemble of 39 simulations with the CCSM3, a fully coupled non-flux-adjusted model with atmosphere, ocean, land, and sea ice components. Various aspects of the CCSM3 and its twenty-first-century response to several Special Report on Emissions Scenarios (SRES) forcing trajectories are described in Collins et al. (2006) and Meehl et al. (2006), respectively. As described in Deser et al. (2012b), each member of this large CCSM3 ensemble is subject to the same SRES A1B external forcing scenario during the twenty-first century and identical initial conditions in the ocean, sea ice, and land component models obtained from 1 January 2000 at the end of a separate CCSM3 twentieth-century simulation. The 39 different ensemble members were generated by initializing CCSM3's atmospheric component model (CAM3) with atmospheric conditions obtained from different days surrounding 1 January 2000 at the end of the twentieth-century simulation. The 39-member ensemble uses CAM3 at a T42 horizontal resolution (triangular spectral truncation at a total wavenumber of 42; equivalent to 2.8° resolution in latitude and longitude) and 26 levels in the vertical. With the exception of an excluded 40th ensemble member that was found to have some corrupted output fields, it is the same ensemble used by Deser et al. (2012a,b) and a superset of the one used by Hu et al. (2012). More information on this unique large CCSM3 ensemble, especially regarding climate predictability, is available in Branstator and Teng (2010) and Teng and Branstator (2011).

Smaller (seven or fewer member) ensembles from CCSM4 that incorporate the newly released Community Atmosphere Model, version 4 (CAM4), at a nominal horizontal resolution of 1° are used to assess the robustness of CCSM3 results. Key CCSM4 features and its response to various representative concentration pathway (RCP) external forcing scenarios are described in Gent et al. (2011) and Meehl et al. (2012), respectively.

Satellite-based sea ice observations and an atmospheric reanalysis product are used to assess the applicability of the model results to nature. September Arctic sea ice extent for 1979–2010 is obtained digitally from the National Snow and Ice Data Center (NSIDC; Fetterer et al. 2002, with updates). We calculated monthly-mean ice velocities for 1980–2006 from daily data retrieved by the National Aeronautic and Space Administration's (NASA) Polar Pathfinder satellite (Fowler 2003, with updates). Monthly-mean sea level pressure (SLP) and 1000-hPa winds for 1980–2010 are obtained from the European Center for Medium-Range Weather Forecasts (ECMWF) Interim Re-Analysis (ERA-Interim) product (Simmons et al. 2007, with updates).

We use two complementary indices of summer sea ice amount: September extent and July–November (JASON) volume. The two metrics emphasize different aspects of sea ice variability. In particular, the September extent time series contains relatively more interannual variability compared to the more slowly evolving JASON volume record (not shown). The JASON averaging period is chosen based on the high ($>0.6$) month-to-month autocorrelation of high-pass filtered volume time series within this season; similar results are also obtained, however, using September volume (not shown). Ice extent is defined as the total area ($km^2$) of Arctic grid cells with at least 15% sea ice concentration. In the models as in observations, Arctic sea ice is consistently least extensive during September and the largest ice extent loss trends also occur during September. Summation calculations for both September ice extent and JASON ice volume are performed using the native irregular grid of the component sea ice model to avoid substantial errors associated with spatial smoothing.

The T42 resolution CCSM3 simulates sea ice that is too thick and extensive during the late twentieth century relative to observations (DeWeaver and Bitz 2006). Because of this, we begin our analysis in the year 2020 when the simulated sea ice is more realistic and we

examine trends over the 40-yr period 2020–59. As CCSM4 simulates a more realistic sea ice distribution than CCSM3 (Jahn et al. 2012), we analyze 2010–49 output from that model by applying similar considerations to those described above for CCSM3. We will discuss the influence of different climatological-mean sea ice distributions in section 3 when we compare results from CCSM3 with those from observations and CCSM4.

A few terms are defined here to save space and avoid confusion. *Extent* (EXT) refers to simulated September Arctic sea ice extent and *volume* (VOL) refers to simulated JASON Arctic sea ice volume during the 40-yr intervals described above for CCSM3 and CCSM4. Whether we use linear 40-yr trends or interannual variability, the associated extent and volume indices have been consistently multiplied by $-1$ so that larger (smaller) values indicate greater (lesser) ice loss. Geopotential heights at 1000 and 500 hPa are denoted as $Z_{1000}$ and $Z_{500}$, respectively. Zonal wind at 200 hPa is denoted as $U_{200}$ and near-surface reference air temperature is denoted as $T_{\mathrm{ref}}$.

This paper focuses on internal variability in summer Arctic sea ice loss by analyzing the spread of trends across the ensemble. The terms *ensemble trend regression* and *ensemble trend correlation* will be shorthand for regressions onto and correlations with the 39 standardized 2020–59 EXT or VOL linear trend values obtained from the CCSM3 ensemble. These ensemble trend regressions and ensemble trend correlations therefore describe relationships between internal variability in the trends of various fields and the internal variability in sea ice loss trends. All results based on linear trends are similar to those based on epoch differences (not shown).

Empirical orthogonal function (EOF)—principal component (PC) analysis is used to characterize the leading patterns of $Z_{1000}$, $Z_{500}$, and $T_{\mathrm{ref}}$ trend variability across the CCSM3 ensemble. Unlike conventional EOF and PC analysis applied to the time domain, we apply the method to the ensemble member trend domain (see also Deser et al. 2012b). That is, the set of 39 different 2020–59 trend maps are subjected to EOF and PC analysis. We refer to the resulting spatial patterns as EOFs and the 39 weights for each spatial pattern as PCs. Note that by construction, the ensemble-mean trends are removed in the EOF and PC analysis. All EOF and regression patterns are displayed in physical units per standard deviation of the reference index (e.g., PC, EXT, or VOL).

## 3. Results

This section is structured as follows. First, we assess the magnitude of the spread in projected Arctic sea ice loss across the 39-member CCSM3 ensemble, spread that is by definition attributable to internal variability (section 3a). Then we explore the role of the atmospheric circulation in driving internal variability in sea ice loss trends, paying particular attention to their spatial pattern, seasonal dependence, and imprint upon ice advection (section 3b). To help validate the model results, we compare the relationships between atmospheric circulation and Arctic sea ice variability on interannual time scales in CCSM3, CCSM4, and observations (section 3c). Finally, we examine the global signature of the atmospheric circulation patterns that drive sea ice loss trends and explore to what extent they represent dominant structures of variability in their own right, independent of their relationship to Arctic sea ice (section 3d).

### a. *The importance of internal variability on projections of twenty-first-century Arctic sea ice loss*

The importance of internal variability on projections of twenty-first-century Arctic sea ice loss is demonstrated in Fig. 1. Averaged across the 39 members, CCSM3 exhibits an ensemble-mean ice loss trend of $4.1 \times 10^6\,\mathrm{km}^2$ in EXT and $13 \times 10^3\,\mathrm{km}^3$ in VOL over the 2020–59 period. These ensemble-mean trends provide an estimate of the GHG-forced signal in Arctic sea ice loss. However, individual ensemble members can differ markedly from the ensemble mean because of the superposition of internally generated and externally forced trends. In fact, the EXT and VOL trends range by nearly a factor of 3 (from $-2.0 \times 10^6$ to $-5.7 \times 10^6\,\mathrm{km}^2$ in EXT and from $-7.0 \times 10^3$ to $-19 \times 10^3\,\mathrm{km}^3$ in VOL) across the ensemble, indicating the substantial contribution of internal variability to future Arctic sea ice loss (Fig. 1, top). The 2020–59 trend values have a standard deviation (range) of $0.83 \times 10^6\,\mathrm{km}^2$ ($3.7 \times 10^6\,\mathrm{km}^2$) and $2.7 \times 10^3\,\mathrm{km}^3$ ($12 \times 10^3\,\mathrm{km}^3$) in EXT and VOL, respectively. Note that each ensemble member is a plausible simulation of the future trajectory of Arctic sea ice loss according to CCSM3.

Figure 1 (top) illustrates the time series of EXT and VOL for the ensemble members with the smallest and largest trends. Not only do the 2020–59 trends differ markedly (see histograms), but large interannual and decadal-scale excursions about the ensemble-mean trend are evident (note the higher proportion of low-frequency variability in the VOL time series compared to the EXT time series). Internal variability therefore has a discernible influence over a wide range of time scales. There is little evidence in these time series for the development of a strong internal positive feedback whereby a chance negative or positive departure from the ensemble-mean trend either persists over the long term or amplifies as time

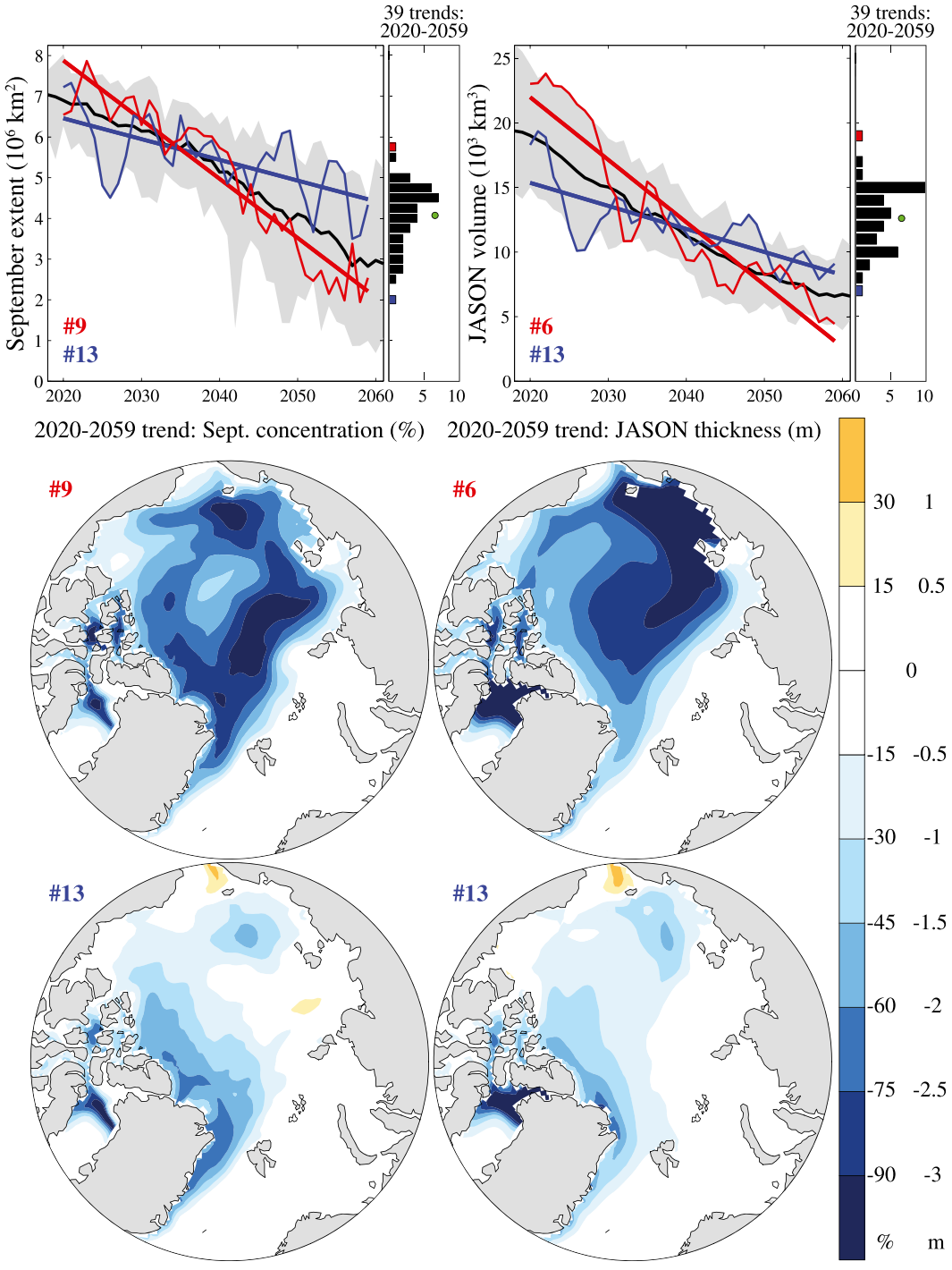


FIG. 1. (top) Time series of the ensemble mean (black line), ensemble range (gray shading), and the individual ensemble members with the smallest (blue lines) or largest (red lines) 2020–59 loss in Arctic (top left) September sea ice EXT and (top right) July–November (JASON) sea ice VOL. Histograms to the right of the top panels display the 2020–59 ice loss trend distribution on the same vertical axis as the time series. Two small green dots indicate the ensemble-mean ice loss trends in EXT and VOL. (middle),(bottom) Maps show the 2020–59 (left) ice concentration or (right) thickness trends for the individual ensemble members with the largest and smallest trends in ice EXT or VOL loss, respectively. The largest (smallest) trend in September ice EXT loss of $5.7 \times 10^6$ km$^2$ ($2.0 \times 10^6$ km$^2$) is experienced by ensemble member 9 (13), as indicated. The largest (smallest) trend in JASON ice VOL loss of $19 \times 10^3$ km$^3$ ($7.0 \times 10^3$ km$^3$) is experienced by ensemble member 6 (13), as indicated. A scale for the 2020–59 trend maps in September ice concentration (%) and JASON ice thickness (m) is indicated alongside the colorbar.

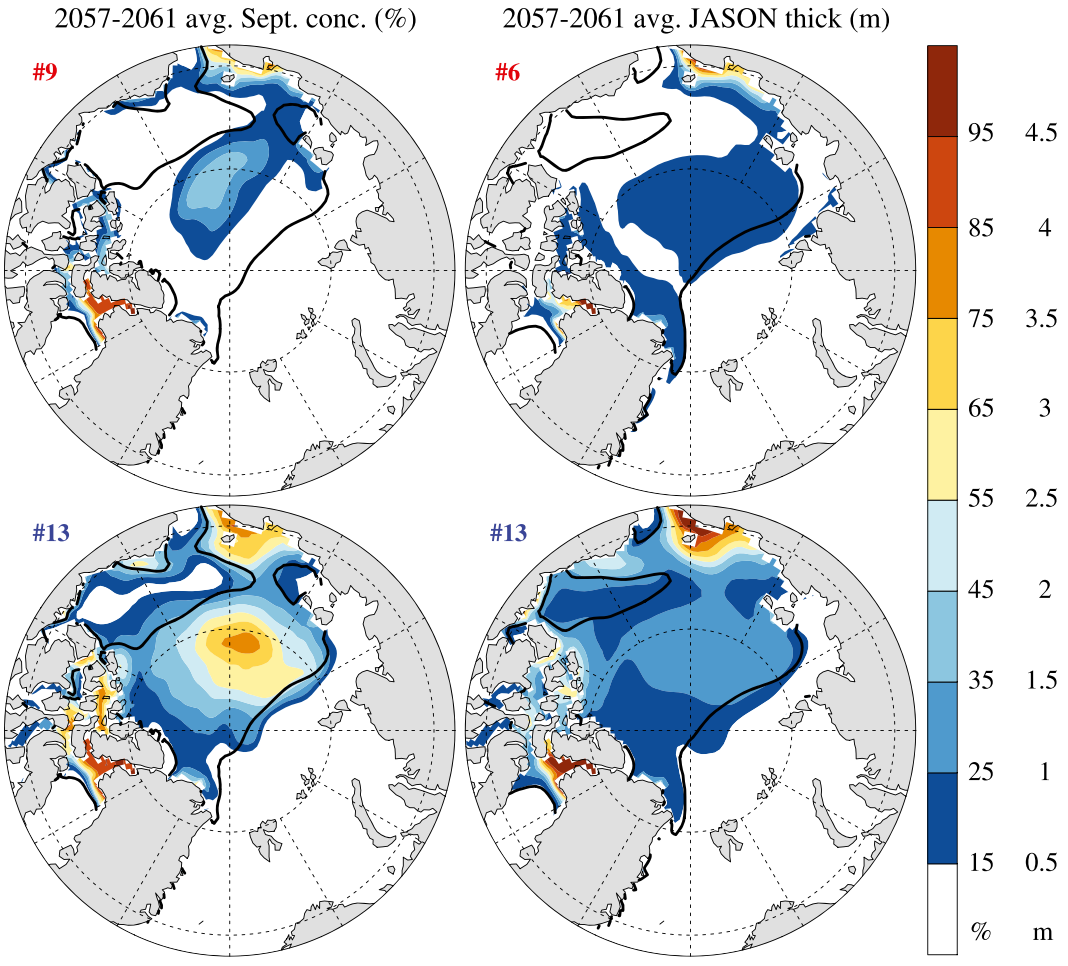


FIG. 2. The 5-yr average 2057–61 (left) September ice concentration and (right) JASON ice thickness from the individual ensemble members with the (top) largest and (bottom) smallest 40-yr trend in ice EXT or ice VOL, respectively. The ensemble-mean 15% ice concentration and 0.5-m ice thickness isopleths are contoured in black.

progresses. Mechanisms other than those directly associated with GHG forcing and the associated feedbacks contribute importantly to the magnitude of 40-yr Arctic sea ice loss trends in CCSM3.

Sea ice concentration and thickness trend maps are also shown in Fig. 1 for the ensemble members with the largest and smallest EXT and VOL trends. Although substantial ice concentration and thickness losses occur in all ensemble members, they tend to be smaller and concentrated around Greenland and the Canadian Archipelago in the ensemble members with the least sea ice loss (Fig. 1, bottom maps) and larger and spread throughout the central and eastern Arctic in the ensemble members with the most sea ice loss (Fig. 1, top maps).

The amount and distribution of sea ice averaged over the last five years of the simulation period (2057–61) are illustrated for the same ensemble members in Fig. 2. Ensemble members with relatively large ice loss trends exhibit mostly ice-free conditions in the central Arctic by 2057–61 (Fig. 2, top). The ensemble members with relatively small ice loss trends retain substantially more extensive, more concentrated, and thicker sea ice in both the central Arctic and the East Siberian Sea (Fig. 2, bottom). These results illustrate that the concentration and thickness of summer Arctic sea ice cover remaining in the mid-twenty-first century is subject to considerable uncertainty as a result of internal climate variability.

In summary, the magnitude of Arctic sea ice loss projected to occur during 2020–59 is influenced not only by the buildup of GHGs but also by internal variability. This internal variability can augment or diminish the GHG-induced ice loss in any individual model realization. Intrinsic amplification mechanisms (e.g., positive ice–albedo feedback) acting on randomly generated sea ice anomalies do not dominate the spread in ice loss among the 39 CCSM3 ensemble members.

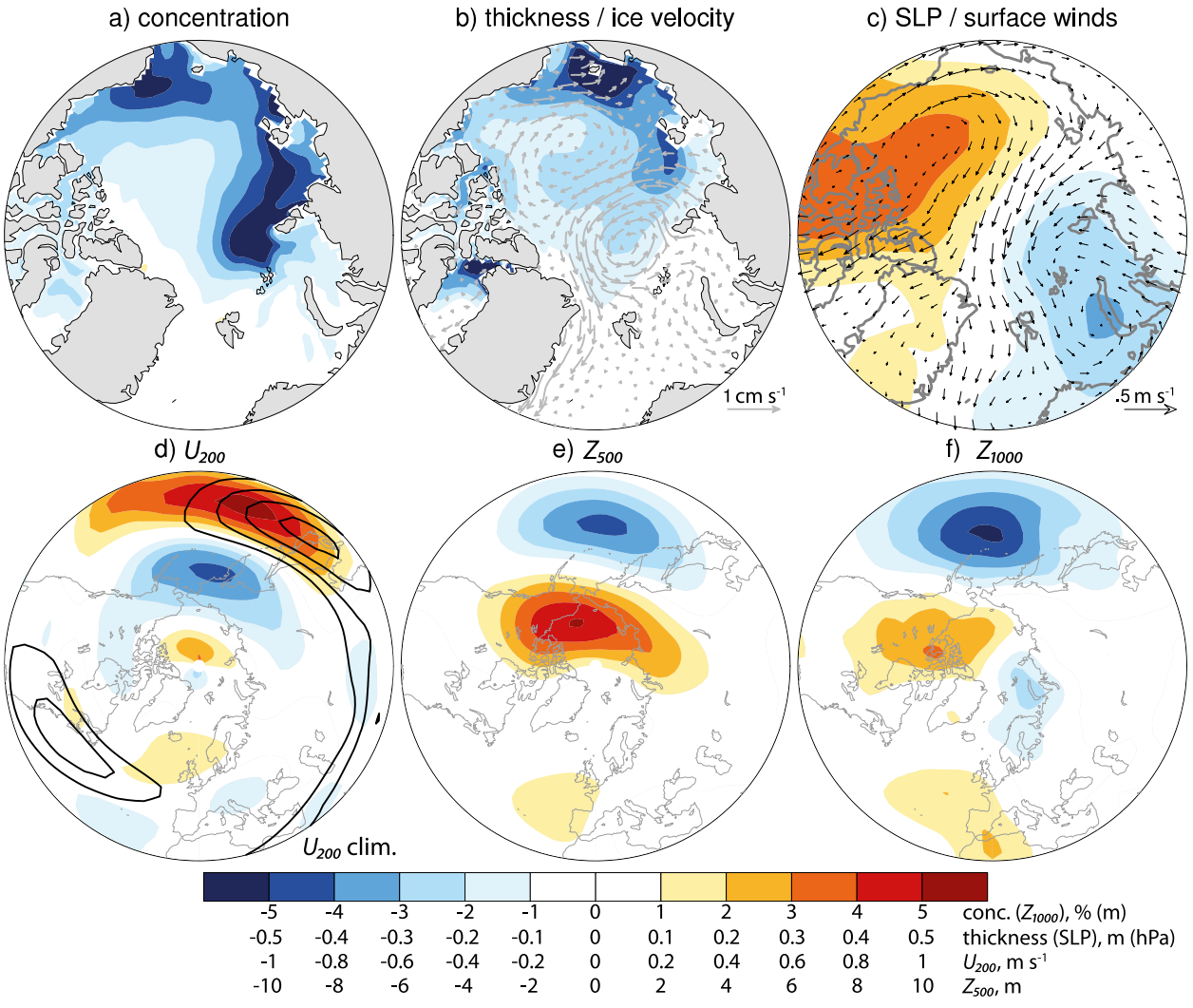


FIG. 3. Ensemble trend regressions between 2020–59 trends in September sea ice EXT and 2020–59 trends in (a) sea ice concentration, (b) sea ice thickness, (c) SLP, (d) $U_{200}$, (e) $Z_{500}$, and (f) $Z_{1000}$. Regressions of (b) sea ice motion and (c) winds in the lowest (surface) atmospheric model layer are also shown along with reference vectors for scale. All ensemble trend regression calculations are based on annual-mean values from October to September to reflect the sea ice year. The EXT trend values are multiplied by −1 so that larger values reflect increased ice loss [see (a) and (b)]. All plotted regression coefficients are per standard deviation ($0.83 \times 10^6$ km$^2$) of the ensemble spread in 2020–59 September Arctic sea ice EXT trends (i.e., the histogram from top left in Fig. 1). The 2020–59 time-mean and ensemble-mean climatology of annual $U_{200}$ is contoured in (d) at 5 m s$^{-1}$ contour intervals starting at 30 m s$^{-1}$ to indicate the location of the midlatitude jet at 200 hPa. Top and bottom panels show relationships poleward of 68° and 30°N, respectively.

### *b. Ice loss, ice advection, and atmospheric circulation*

Ensemble trend regressions are a compact and systematic way to explore relationships between internal variability in the trends of different variables with those in ice loss. Ensemble trend regressions onto EXT are shown for a variety of annually averaged ice and atmospheric variables in Fig. 3. For example, Fig. 3c shows the 40-yr SLP trends that are linearly associated with a one standard deviation change in the 40-yr trend of September Arctic sea ice EXT. Ice concentration and ice thickness ensemble trend regressions (Figs. 3a,b) are largest off the coast of Eurasia and in the eastern Arctic, a pattern that qualitatively matches the spatial distribution of concentration and thickness trend differences between the ensemble members with the largest and smallest ice loss trends (recall Fig. 1). Ice velocity ensemble trend regressions onto EXT indicate a coherent pattern of sea ice advection that originates off the Siberian coast, crosses the central Arctic, and exits the Arctic through the Fram Strait and Barents Sea (Fig. 3b). This "transpolar" ice advection is coherent with near-surface

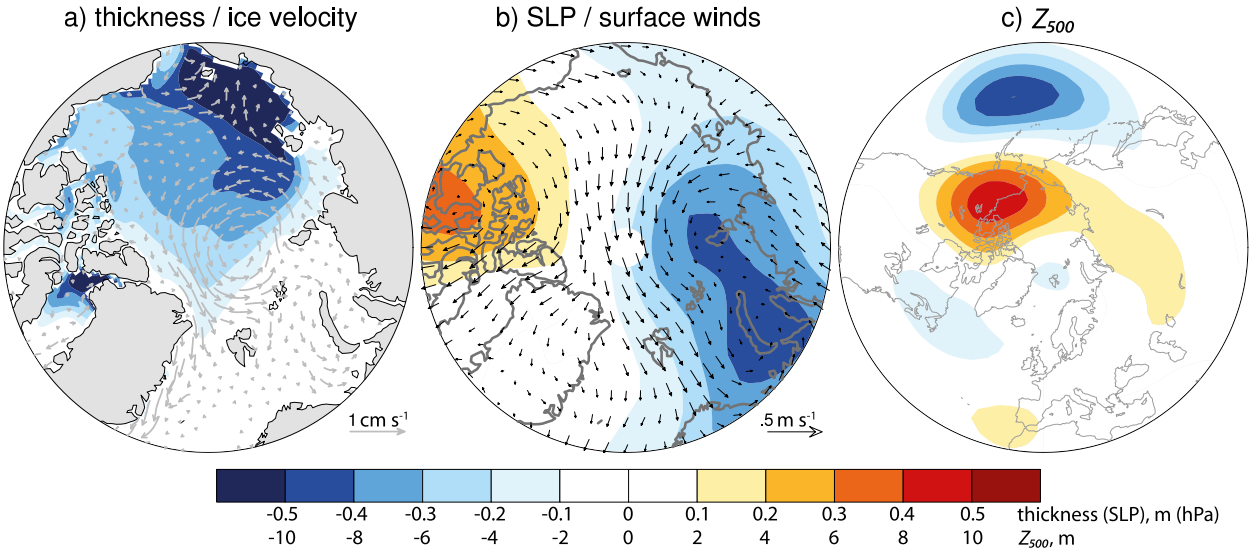


FIG. 4. As in Fig. 3, but for 2020–59 trends in annual (a) ice thickness and ice velocity, (b) SLP and near-surface wind, and (c) $Z_{500}$ fields regressed onto the standardized ensemble spread in 2020–59 JASON Arctic sea ice VOL trends instead of September sea ice EXT trends. Reference vectors indicating a regression value of 1 cm s$^{-1}$ and 0.5 m s$^{-1}$ per standard deviation ($2.7 \times 10^3$ km$^3$) are shown for scale next to the ice velocity and surface wind regression maps, respectively. Relationships poleward of 68°N are shown in (a) and (b) and relationships poleward of 30°N are shown in (c).

atmospheric winds that are in turn associated with a SLP gradient between the western and the eastern Arctic (Fig. 3c). The ensemble trend regression in SLP is reminiscent of the dipole anomaly/Arctic dipole (AD) described by Wu et al. (2006) and Overland and Wang (2010). The pattern of ice thickness ensemble trend regression coefficients appears to be associated with the ice velocity field in the central Arctic, as evidenced for example by the two lobes in the ice thickness regression map that straddle the strongest central Arctic ice velocities and also by the weak tongue of ice thickness regression coefficients extending toward the Fram Strait region of ice export.

Expanding our analysis domain to 30°N, ensemble trend regressions illustrate a coherent pattern of atmospheric circulation covariability with EXT from the level of the subtropical jet ($U_{200}$, Fig. 3d), through the midtroposphere ($Z_{500}$, Fig. 3e), and down to the surface ($Z_{1000}$, Fig. 3f). Extratropical atmospheric covariability is concentrated into a geopotential height dipole pattern over the Pacific sector with centers of action in the subpolar Arctic and in the midlatitude North Pacific (Figs. 3e,f). The vertical structure of this pattern appears to be largely equivalently barotropic (Figs. 3d–f). (Corresponding ensemble trend correlations with EXT are shown in Fig. A1 of the appendix.)

A subset of the ensemble trend regression maps from Fig. 3 are repeated in Fig. 4 using VOL trends as the index variable. Ice advection in these VOL-based regression maps is qualitatively similar to the analysis based on EXT, but sea ice velocity regression coefficients are relatively more concentrated into a gyre-like circulation near the North Pole. In addition, sea ice thickness regression coefficients are stronger throughout the central Arctic and extend more obviously into a Fram Strait tongue (Fig. 4a). The dipole pattern in the SLP ensemble trend regression onto VOL places more emphasis on the eastern side of the Arctic, but the magnitudes of the SLP gradient and associated surface wind regressions across the central Arctic (Fig. 4b) are comparable to those based on EXT (Fig. 3c). The $Z_{500}$ ensemble trend regression onto VOL (Fig. 4c) is slightly stronger over the central North Pacific than the comparable regression onto EXT (Fig. 3e). Overall, the $Z_{500}$ ensemble trend regression onto VOL is suggestive of a Rossby wave train emanating from the midlatitude central Pacific. All of the atmospheric ensemble trend regression patterns associated with VOL are rotated roughly 30° counterclockwise (eastward) relative to those associated with EXT (cf. Figs. 4b,c with Figs. 3c,e). In general, the $Z_{500}$ ensemble trend regression onto VOL in Fig. 4c provides a more compelling link to the midlatitudes than the analogous regression onto EXT in Fig. 3e in that the North Pacific lobe is more intense and more coherently linked to a downstream Rossby wave train. We will return to a comparison of the EXT and VOL patterns of atmospheric covariability in the discussion.

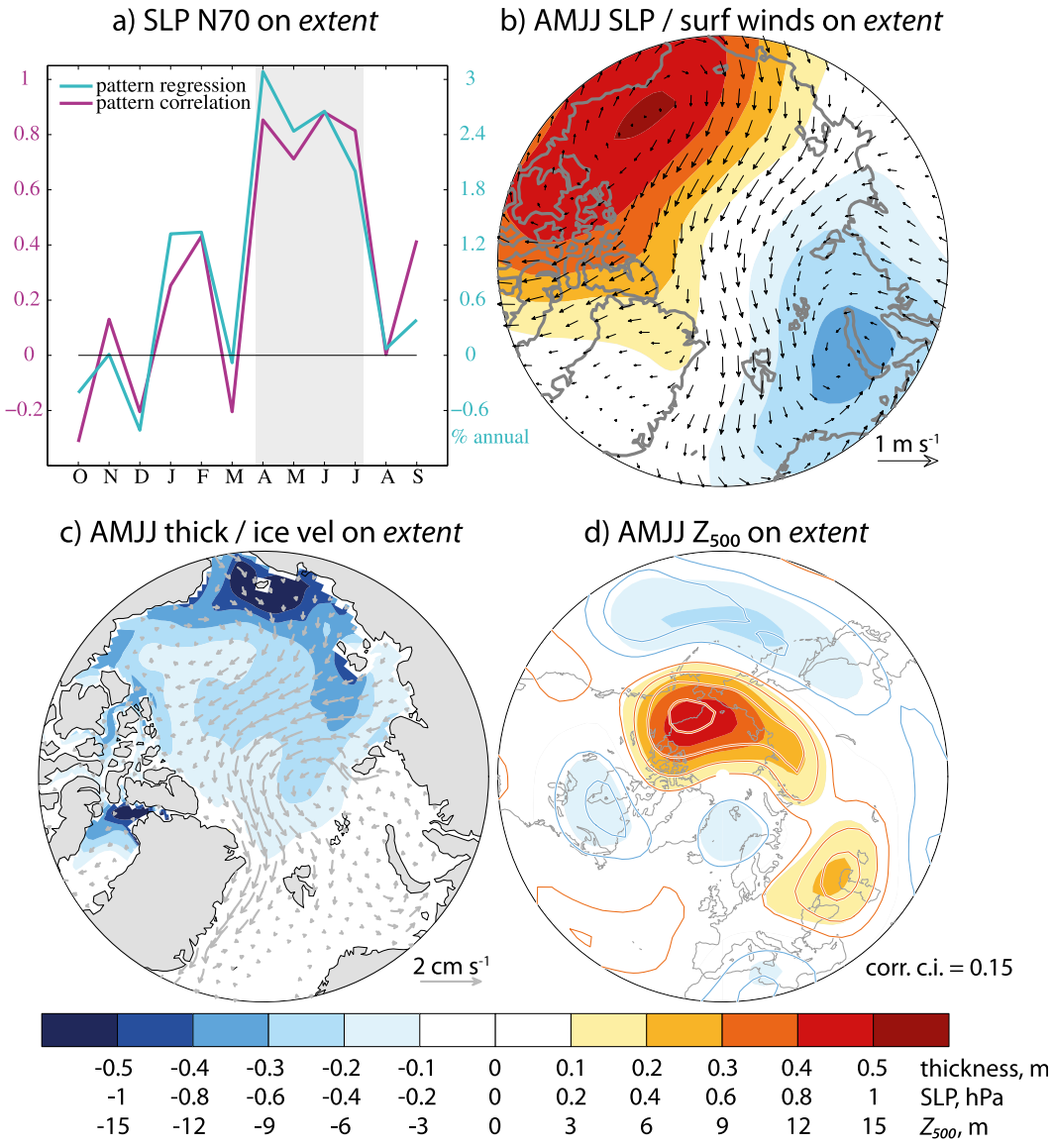


FIG. 5. (a) Seasonality of 2020–59 SLP ensemble trend regressions onto EXT (see text for details). Pattern correlation magnitudes are indicated on the left axis and pattern regression magnitudes normalized to the annual-mean AD regression map (Fig. 3c) are indicated on the right axis. AMJJ regressions of (b) SLP and near-surface wind, (c) sea ice thickness and ice velocity, and (d) $Z_{500}$ (color shading) are shown per standard deviation ($0.83 \times 10^6$ km$^2$) of the ensemble spread in 2020–59 September Arctic sea ice EXT trends. Corresponding AMJJ ensemble trend correlation coefficients between $Z_{500}$ and EXT are also shown [see (d); contours] to enhance comparability with Figs. 6b and A1e. Relationships poleward of 68°N are shown in (b) and (c), whereas relationships poleward of 30°N are shown in (d).

To assess the seasonal dependence of the atmospheric circulation ensemble trend regressions on EXT (and volume), we compute area-weighted pattern correlations and pattern regressions between the annual ensemble trend regression maps of Fig. 3c (Fig. 4c) and similar ensemble trend regression maps calculated using monthly atmospheric trends. Pattern correlations and regressions are performed poleward of 70°N for SLP and poleward of 30°N for $Z_{500}$.

The annual-mean Arctic dipole–like SLP association with EXT (Fig. 3c) is concentrated between April and July (AMJJ; Fig. 5a), and the corresponding AMJJ SLP and surface wind ensemble trend regression patterns (Fig. 5b) are roughly twice as strong as in the annual mean (Fig. 3c). The transpolar drift in ice velocity (Fig. 5c) is also more intense during AMJJ and more clearly associated with ice advection away from the Eurasian coast than in the annual average (Fig. 3b). Finally, the AMJJ

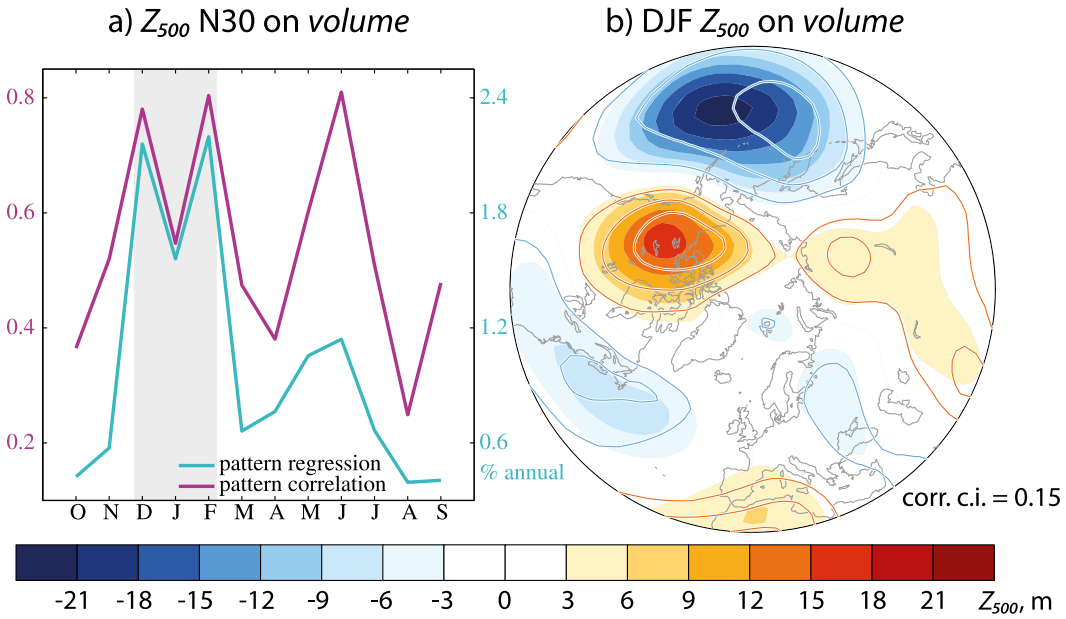


FIG. 6. (a) Seasonality of 2020–59 $Z_{500}$ ensemble trend regressions onto VOL (see text for details). Pattern correlation magnitudes are indicated on the left axis and pattern regression magnitudes normalized to the annual-mean Rossby wave train regression map (Fig. 4c) are indicated on the right axis. (b) December–February (DJF) regressions of $Z_{500}$ (color shading) are shown per standard deviation ($2.7 \times 10^3$ km$^3$) of the ensemble spread in 2020–59 JASON Arctic sea ice VOL trends. Corresponding DJF ensemble trend correlation coefficients between $Z_{500}$ and VOL are also shown (contours) to enhance comparability with Fig. 5d. Relationships poleward of 30°N are shown in (b).

$Z_{500}$ ensemble trend regression and ensemble trend correlation patterns (Fig. 5d) emphasize the central Arctic lobe of a Pacific Rossby wave train compared to the annual-mean regressions (Fig. 3e) and correlations (Fig. A1e). It is noteworthy that the ensemble trend regression of AMJJ $Z_{500}$ on EXT (Fig. 5d) bears considerable similarity to the observed $Z_{500}$ anomalies in the months preceding the previous record minimum Arctic sea ice extent in 2007 [e.g., Fig. 3a in L'Heureux et al. (2008)].

The annual-mean association between VOL trends and the $Z_{500}$ Rossby wave train in the Pacific sector (Fig. 4c) is concentrated from December to February (DJF), with a secondary maximum in the pattern correlation during June. However, the pattern regression (i.e., the relationship between the annual and monthly ensemble trend regression patterns in physical units) is substantially weaker in June than in DJF (Fig. 6a). The DJF $Z_{500}$ ensemble trend regression pattern exhibits a pronounced Pacific Rossby wave train (Fig. 6b) that is more than twice as strong as in the annual average (Fig. 4c). The interpretation of this pattern as a Rossby wave train emanating from the Pacific is supported by the fact that the strongest center of action in Fig. 6b occurs over the North Pacific and weaker centers occur downstream over northwest Canada and off the east coast of North America.

It is worth noting that although the ensemble trend regressions of $Z_{500}$ onto VOL emphasize the Rossby wave train pattern during the DJF season, weaker but consistently positive pattern correlations and regressions exist in all months of the year (Fig. 6a). Compared to DJF, the $Z_{500}$ Rossby wave train pattern associated with extent trends during AMJJ (Fig. 5d) exhibits a shorter length scale (higher wavenumber), and its strongest center of action is in the Arctic instead of the North Pacific.

### c. *Interannual atmospheric forcing of sea ice loss in CCSM3, observations, and CCSM4*

Prior subsections have described covarying trends of sea ice and atmospheric circulation within the 39-member CCSM3 ensemble. This subsection explores to what extent similar relationships may be found at interannual time scales not only within the CCSM3 ensemble, but also in observational products and within smaller CCSM4 ensembles.

Lead–lag bimonthly regressions of $Z_{1000}$, $Z_{500}$, ice velocity, and ice thickness onto a 1-yr differenced VOL time series are shown in Fig. 7. Each regression map is based on 1560 time points resulting from the concatenation of time series during 2020–59 across the 39 ensemble members. The 1-yr differencing serves as an effective high-pass filter to remove the strong trend

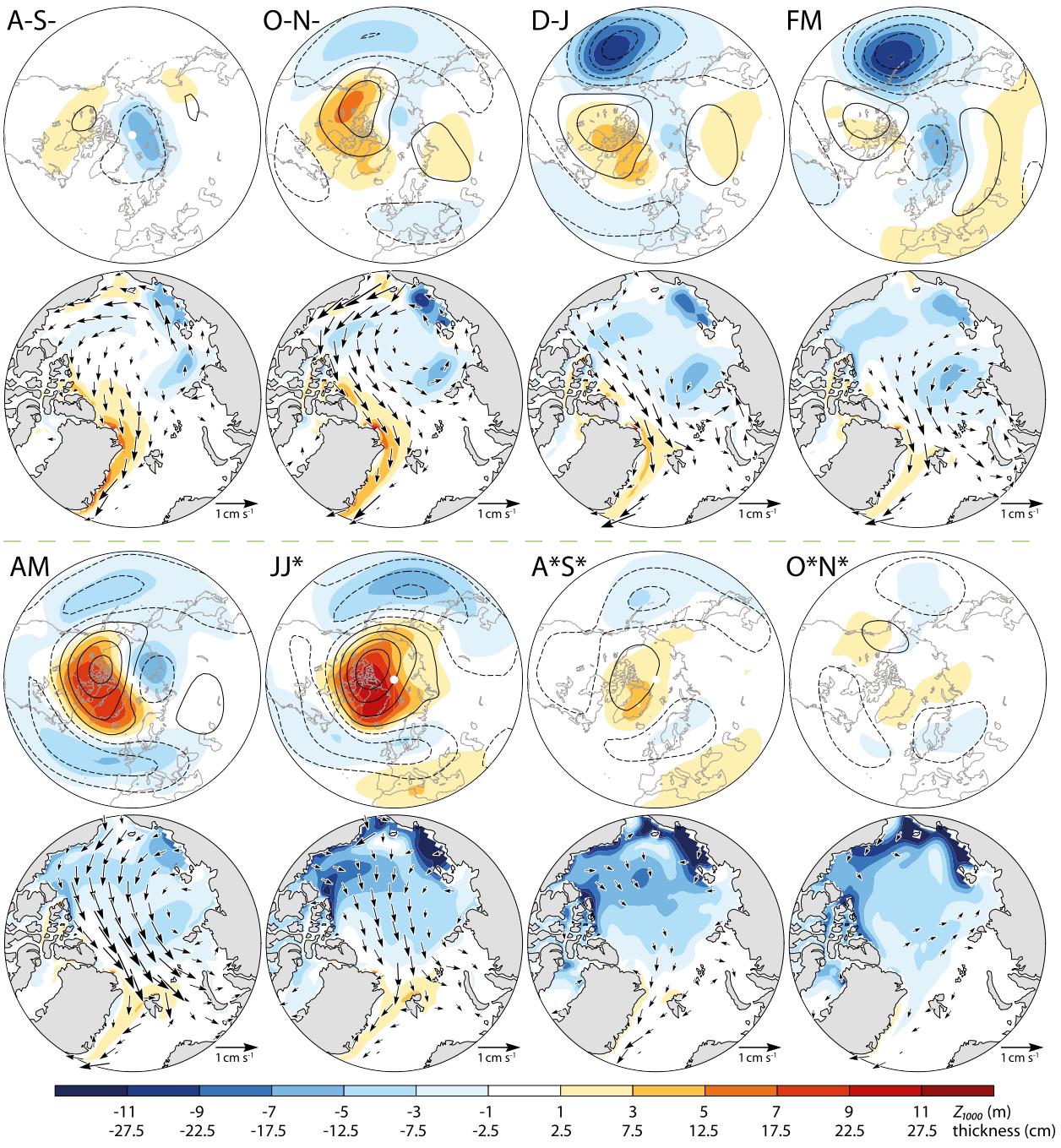


FIG. 7. Lead–lag 2020–59 bimonthly regressions onto standardized 1-yr differenced values of the JASON ice volume. (top) The $Z_{1000}$ (color shading) and $Z_{500}$ (contours; contour interval 4 m) regressions onto the JASON ice volume time series. (bottom) Ice velocity (vectors) and 1-yr differenced ice thickness (color shading) regressions onto the same JASON ice volume time series. Time advances as one reads column by column from upper left to lower right. Regressions are for the 2-month averages indicated in the upper left of each top row panel (e.g., August–September is denoted AS). Regressions leading and in the year prior to the JASON VOL index are denoted with a negative sign (e.g., A-S− indicates results are based on 2019–58 August–September averages). The JASON months that are synchronous with the index are indicated with an asterisk. The JASON ice VOL time series and all spatial regressions are composed of 1560 time points (40 yr × 39 ensemble members). The contour interval for $Z_{1000}$ (m) and ice thickness (cm) regressions is indicated below the colorbar. Reference vectors indicating 1 cm $s^{-1}$ ice velocity regressions are indicated at the bottom right of each panel containing such regressions. Vectors representing ice velocities below 0.2 cm $s^{-1}$ and the spurious ice velocity regressions at the sea ice edge are excluded for clarity. Geopotential height regressions are shown poleward of 30°N, whereas ice velocity and thickness regressions are shown poleward of 68°N.

component from the raw VOL time series, and it is also physically motivated, given that the observed time tendency in the amount of summer Arctic sea ice is influenced by the overlying atmospheric circulation and associated with wind-driven ice advection (e.g., see papers cited in the introduction). The 1-yr differencing of the ice thickness time series at each gridpoint and regressing these onto the 1-yr differenced VOL time series provides an indication of the evolving spatial distribution of high-pass filtered ice thickness anomalies associated with high-pass filtered VOL changes. Unfiltered and high-pass filtered $Z_{1000}$, $Z_{500}$, and ice velocity regressions onto the 1-yr differenced VOL time series yield similar results (not shown); the results based on unfiltered data are displayed in Fig. 7 as a more straightforward indicator of the patterns of atmospheric covariabilty ($Z_{1000}$ and $Z_{500}$) and the response in ice advection (ice velocity).

The spatial patterns and seasonal evolution of the high-pass filtered atmospheric circulation regression maps are similar to those of the ensemble trend regression maps (e.g., compare Fig. 7 with Figs. 5 and 6). In particular, the predominance of negative geopotential height regression coefficients over the North Pacific with downstream centers of action resembling a Rossby wave train in December through March evolves into an Arctic-concentrated mostly annular structure by June–July (Fig. 7). A weak equivalent barotropic North Pacific low pressure center exists already in October–November of the year preceding the summer sea ice VOL index. A weak Arctic dipole–like pattern in central Arctic $Z_{1000}$ regression coefficients is also already present in October–November, and this pattern persists through February–March and then strengthens substantially in April–May. Positive geopotential height regression coefficients fill the Arctic basin in June–July, but a similar east–west SLP gradient persists across the Arctic because the strongest positive SLP anomalies are positioned over the western Arctic. After July, central Arctic geopotential height regression coefficients weaken substantially. Note that the evolution in atmospheric circulation associated with Fig. 7 is strictly only related to sea ice covariability and that a separate analysis of the atmospheric variability would be necessary to link the evolution of the various patterns dynamically.

Ice export across the central Arctic through the Fram Strait and into the Barents Sea occurs throughout the year preceding the summer sea ice VOL index, but the distribution of the central Arctic ice velocity pattern evolves through the year (Fig. 7). The evolving ice velocity pattern is consistently and coherently linked to the distribution and intensity of near-surface winds (not shown but they can be inferred from the $Z_{1000}$ gradient). Ice velocity seems to lead associated anomalies in ice thickness by a month or two (cf. the divergence of the ice velocity field with the development of ice thickness anomalies in the subsequent bimonthly regression map), suggesting that ice advection influences the overall evolution of ice thickness anomalies in the central Arctic. For example, the divergence of the ice velocity field especially in the western Arctic during April–May can be associated with thinner ice in the same area during June–July. Ice export from the central Arctic ceases by the end of September, consistent with the slackening of surface winds and weaker $Z_{1000}$ gradients. The pattern of ice thickness anomalies during October–November at the end of the bimonthly lagged regressions (lower right panel of Fig. 7) is qualitatively similar to the pattern resulting from ensemble trend regressions of ice thickness onto VOL in Fig. 4a.

The results shown in Fig. 7 can be summarized in a few key points. First, the patterns and seasonality of atmospheric circulation covariability with Arctic sea ice loss are generally similar between high-pass filtered and trend-based analyses. Second, ice advection out of the central Arctic is a consistent feature in the bimonthly lead–lag analysis and is itself directly related to the overlying Arctic atmospheric circulation. Third, ice divergence (convergence) can often be related to subsequent sea ice thickness decreases (increases). Finally, the evolution of sea ice–atmospheric circulation covariability is strongest in the year preceding the summer minimum in Arctic sea ice and becomes relatively weak by the last (contemporary) months of the analysis.

Qualitative similarities in the seasonality and spatial distribution between VOL-based regressions using high-pass filtered data and 40-yr trends suggest that a similar mechanism of wind-driven ice advection is operating over a broad range of time scales. Because of this, we explore the relationships between ice motion and SLP anomalies in the short observational record to validate the model results. Figure 8a shows the observed 1979–2010 September sea ice extent time series in both an unfiltered form (black curve) and after a 1-yr difference filter has been applied (red curve; note that extent is used rather than volume because observational estimates of the latter are less robust than those of the former). AMJJ regressions of near-surface winds and SLP from the ERA-Interim reanalysis and of observed ice velocity onto the observed 1-yr differenced September Arctic sea ice extent time series are shown in Figs. 8b and 8c, respectively. The spatial pattern and seasonality of the observed SLP and wind regressions are broadly similar to those identified by Screen et al. (2011). The large-scale patterns in these observed AMJJ regression maps also bear some resemblance to AMJJ regressions of the same

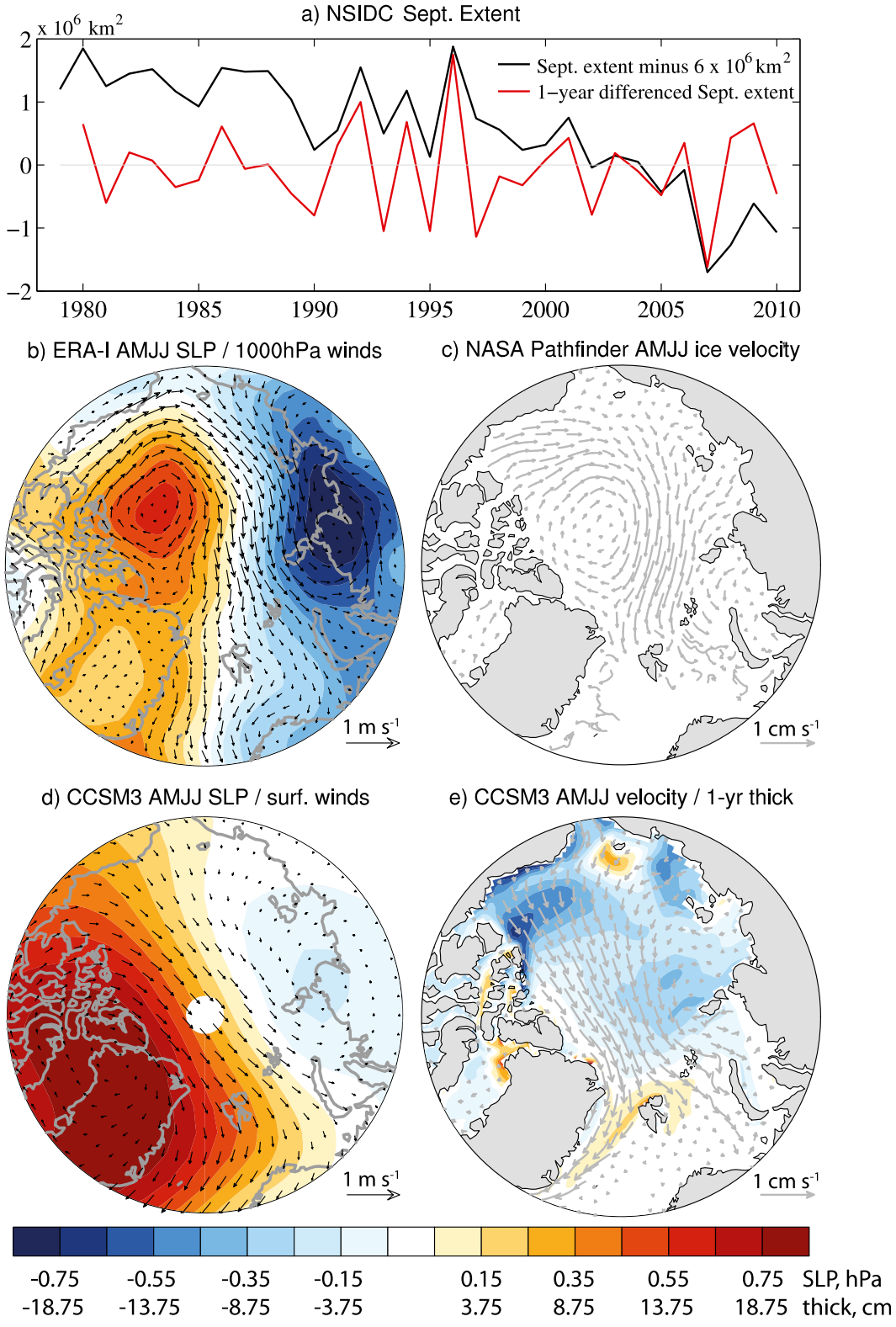


FIG. 8. (a) The unfiltered 1979–2010 September Arctic sea ice extent time series obtained from the NSIDC (black curve) is shown along with the 1-yr differenced time series of the same (red curve). (b) The 31-yr (1980–2010) regression of AMJJ SLP and 1000-hPa winds from the ERA-Interim (ERA-I) reanalysis is shown along with (c) the 27-yr (1980–2006) regression of AMJJ ice velocity from NASA's Polar Pathfinder onto a standardized inverse time series of the red curve in (a). (d),(e) A similar CCSM3 regression onto 1-yr differenced September EXT using 1560 time points from 2020–59 and concatenated across the 39 CCSM3 ensemble members is shown. Ice thickness regression coefficients are included in the CCSM3 analysis shown in (e).

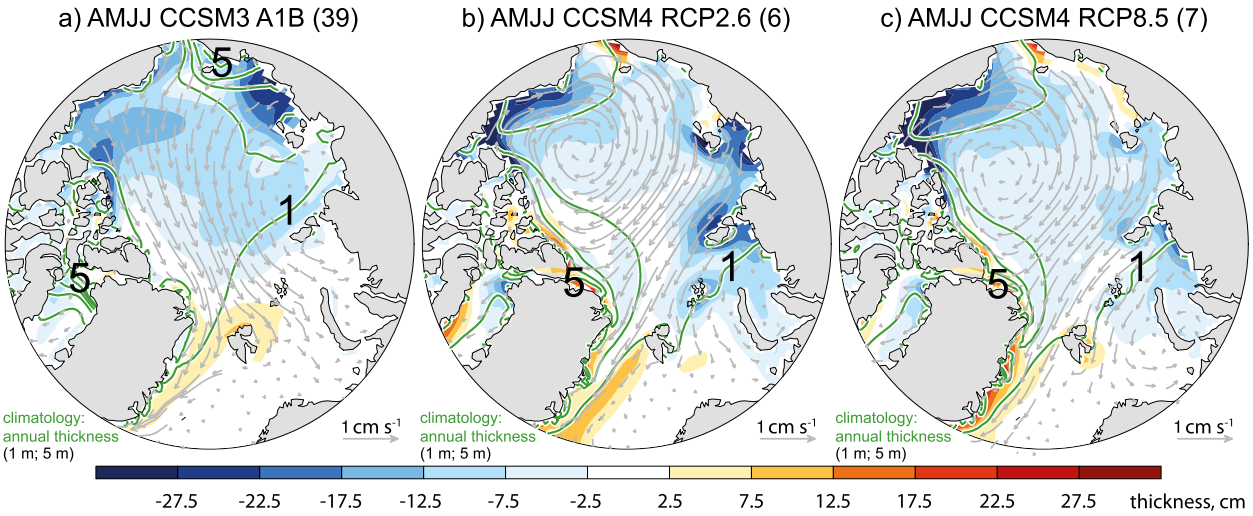


FIG. 9. Regressions of 1-yr differenced AMJJ sea ice thickness (color shading) and unfiltered ice velocity (vectors) onto standardized 1-yr differenced JASON ice VOL (a) in the CCSM3 ensemble and (b),(c) in two of the four CCSM4 RCP ensembles. The CCSM4 ensembles range from relatively weak equivalent GHG forcing (RCP2.6) in (b) to relatively strong equivalent greenhouse gas forcing (RCP8.5) in (c). Each map is based on a concatenation across 40 yr of data and the number of ensemble members indicated in parenthesis. The climatological-, ensemble-, and annual-mean sea ice thickness from the same 40 yr is contoured in green at 1-m intervals up to 5 m. The 1- and 5-m contours are labeled for clarity.

fields onto the concatenated 1-yr differenced EXT time series from CCSM3 (Figs. 8d,e), though differences are sometimes large locally. The AMJJ association with high-pass filtered CCSM3 EXT time series (Figs. 8d,e) can also be compared with the April–May and June–July regression maps onto high-pass filtered CCSM3 VOL time series (Fig. 7, lower left). This comparison indicates that the AMJJ ice thickness regression onto high-pass filtered EXT (Fig. 8e) is associated with a similar seasonal evolution of ice advection to that shown for VOL in Fig. 7. For example, the negative ice thickness anomalies in the Beaufort Sea, the positive anomalies downstream of Wrangel Island, and the positive anomalies in the Fram Strait (Fig. 8e) can all be associated with the evolution of wind-driven sea ice convergence and divergence in the months prior to AMJJ. Although there is an Arctic dipole–like AMJJ SLP gradient associated with Arctic sea ice extent variability in both ERA-Interim (Fig. 8b) and CCSM3 (Fig. 8d), the CCSM3 SLP pattern strongly emphasizes the high over the western Arctic relative to the low over the eastern Arctic. The large-scale pattern of ice motion in CCSM3 (Fig. 8e) is also rotated roughly 30° counterclockwise (eastward) relative to the large-scale pattern of observed NASA Pathfinder ice motion regressed onto observed sea ice extent (Fig. 8c). A transpolar drift in ice velocity culminating in sea ice export through the Fram Strait and into the Barents Sea is, however, a common feature associated with both observed and CCSM3-simulated summer high-pass filtered Arctic sea ice variability, and this extends to variability of 40-yr trends in CCSM3.

Regressions of AMJJ ice velocity and 1-yr differenced AMJJ ice thickness onto 1-yr differenced VOL time series in CCSM3 and CCSM4 are directly compared in Fig. 9. CCSM3 regressions of AMJJ ice velocity and 1-yr differenced ice thickness on 1-yr differenced VOL time series (Fig. 9a) are as expected based on the April–May and June–July bimonthly regressions (Fig. 7, lower left). CCSM4 regressions of the same AMJJ variables in ensembles from both the relatively weak equivalent GHG forcing (RCP2.6; Fig. 9b) and the relatively strong forcing (RCP8.5; Fig. 9c) and also in the intermediate RCP4.5 and RCP6.0 ensembles (not shown) are all associated with a transpolar drift in ice velocity and thickness anomalies that are consistent with an evolution of ice advection away from the coast, across the central Arctic, and out through the Fram Strait and into the Barents Sea.

CCSM4 simulations exhibit a climatological-mean ice thickness distribution that better matches available observations (green contours in Fig. 9; see also Jahn et al. 2012) with thicker ice in the western Arctic compared with the T42 resolution CCSM3 ensemble. The T42 resolution CCSM3 ensemble simulates a bimodal ice thickness distribution with maxima surrounding both the Canadian Archipelago and the coast of the East Siberian Sea. Although AMJJ ice advection and (implied) atmospheric surface pressure regressions are differently distributed in CCSM4 and observations than in

CCSM3, volume loss in each dataset is associated with ice advection away from the coast in the regions of thickest climatological-mean sea ice, a transpolar drift in ice advection through the central Arctic, and ice export through the Fram Strait and into the Barents Sea. Thus, the rotated Arctic dipole–like pattern in CCSM3 compared to observations (Fig. 8) and compared to CCSM4 (Fig. 9) may result from the erroneous climatological-mean distribution of Arctic sea ice in the T42 resolution CCSM3, rather than any particular deficiency in the simulated physical mechanism relating internal variability in Arctic sea ice loss to atmospheric circulation. Equivalently, the better agreement between CCSM4 and the observed distribution of ice advection and (implied) atmospheric surface pressure and surface wind field regressions onto high-pass filtered sea ice variability may result from the better simulation of the climatological-mean Arctic sea ice distribution in CCSM4 than in the T42 CCSM3.

### d. *Atmospheric relationships with internal sea ice trend variability: Intrinsic patterns and global linkages*

Previous subsections have shown that internal variations in Arctic ice loss trends are associated both with an Arctic dipole–like pattern over the central Arctic and also with atmospheric pressure anomalies over the North Pacific. It is interesting to consider whether these constitute intrinsic patterns of variability in their own right, regardless of their association with sea ice. EOF analysis is used to characterize the leading patterns of annual-mean and seasonal-mean $Z_{500}$ and $Z_{1000}$ trend variability in the CCSM3 ensemble (Fig. 10, color shading). The first EOFs of both annual and December–February North Pacific $Z_{500}$ trend variability (Fig. 10, top) are associated with Rossby wave train patterns that bear considerable similarity to, but are stronger than, the comparable $Z_{500}$ ensemble trend regressions onto VOL. Leading EOFs of both annual and April–July $Z_{1000}$ trend variability poleward of 70°N are associated not only with an AD-like pattern over the central Arctic, but also covarying pressure anomalies over the North Pacific (Fig. 10, bottom). The $Z_{1000}$ EOFs in Fig. 10 bear considerable similarity to the comparable $Z_{1000}$ ensemble trend regressions onto EXT. Area-weighted pattern correlations poleward of 30°N between the trend EOFs (color shading) and the ensemble trend regressions onto VOL or EXT (contours in the top and bottom panels, respectively) are in all cases high, ranging between 0.81 and 0.92. It is particularly noteworthy that the 39 PC2 values representing April–July $Z_{1000}$ trend variability (Fig. 10, bottom right) share half of the variance ($r$ = 0.71) with the 39 different values for the 2020–59 EXT trend in the CCSM3 ensemble. Note that the third EOF of $Z_{1000}$ annual trends and the second EOF of $Z_{1000}$ AMJJ trends are displayed, but that each EOF in Fig. 10 is statistically distinct from all other EOFs when the first-order eigenvalue uncertainty estimate described in North et al. (1982) is applied with 39 degrees of freedom. The first EOF of both annual and AMJJ $Z_{1000}$ trends is an Arctic Oscillation–like pattern and the second EOF of annual $Z_{1000}$ trends is a dipole over the Arctic that is mostly associated with North Atlantic variability (not shown). EOF patterns similar to those in Fig. 10 are obtained using $Z_{500}$ and $Z_{1000}$ trends over different spatial domains and within other seasons (not shown). Comparable EOFs are also obtained using a 1000-yr CCSM3 control integration (not shown) and have been obtained in EOF-based analysis of interannual variability in reanalysis (e.g., Overland and Wang 2005; Wu et al. 2006; Wang et al. 2009).

It is worth noting that the trend-based EOF analysis is designed to pick out the leading patterns of annual-mean or seasonal-mean trend variability across the 39 ensemble members independent of any Arctic sea ice relationships. The similarity between these ensemble trend EOFs and the ensemble trend regressions used to identify atmosphere–sea ice covariability suggests that internal variability in the trends of Arctic sea ice loss is associated with naturally occurring patterns of low-frequency atmospheric circulation variability.

The global signature of atmospheric circulation trends associated with internal variability in VOL trends is depicted in Figs. 11 and 12 (similar results are obtained using EXT trends, not shown). Annual-mean geopotential heights averaged over the Pacific sector (120°E–90°W) exhibit ensemble trend correlations and regressions with VOL that extend coherently throughout the depth of the troposphere, with positive values poleward of 55°N and negative values in the midlatitudes (Fig. 11). A weak extension of geopotential height covariability into the tropics is also evident, suggesting a linkage between internal variability in trends of Arctic sea ice and tropical Pacific atmospheric circulation.

Global ensemble trend regression and correlation maps of annual-mean $Z_{500}$, SLP, and $T_{ref}$ onto VOL (left panels, Fig. 12) confirm the extension of ice-related atmospheric trends into the tropics and into the Southern Hemisphere. In particular, internal variability in VOL trends is associated with positive $Z_{500}$ trends throughout the tropics and a SLP trend dipole between the tropical Pacific and Atlantic. A baroclinic structure is evident in the atmospheric pressure anomalies over the central tropical Pacific (cf. Figs. 12a,c). In addition, positive $Z_{500}$ and SLP trends are found over the Pacific sector of the Southern Ocean. These tropical and extratropical features associated with Arctic ice VOL loss

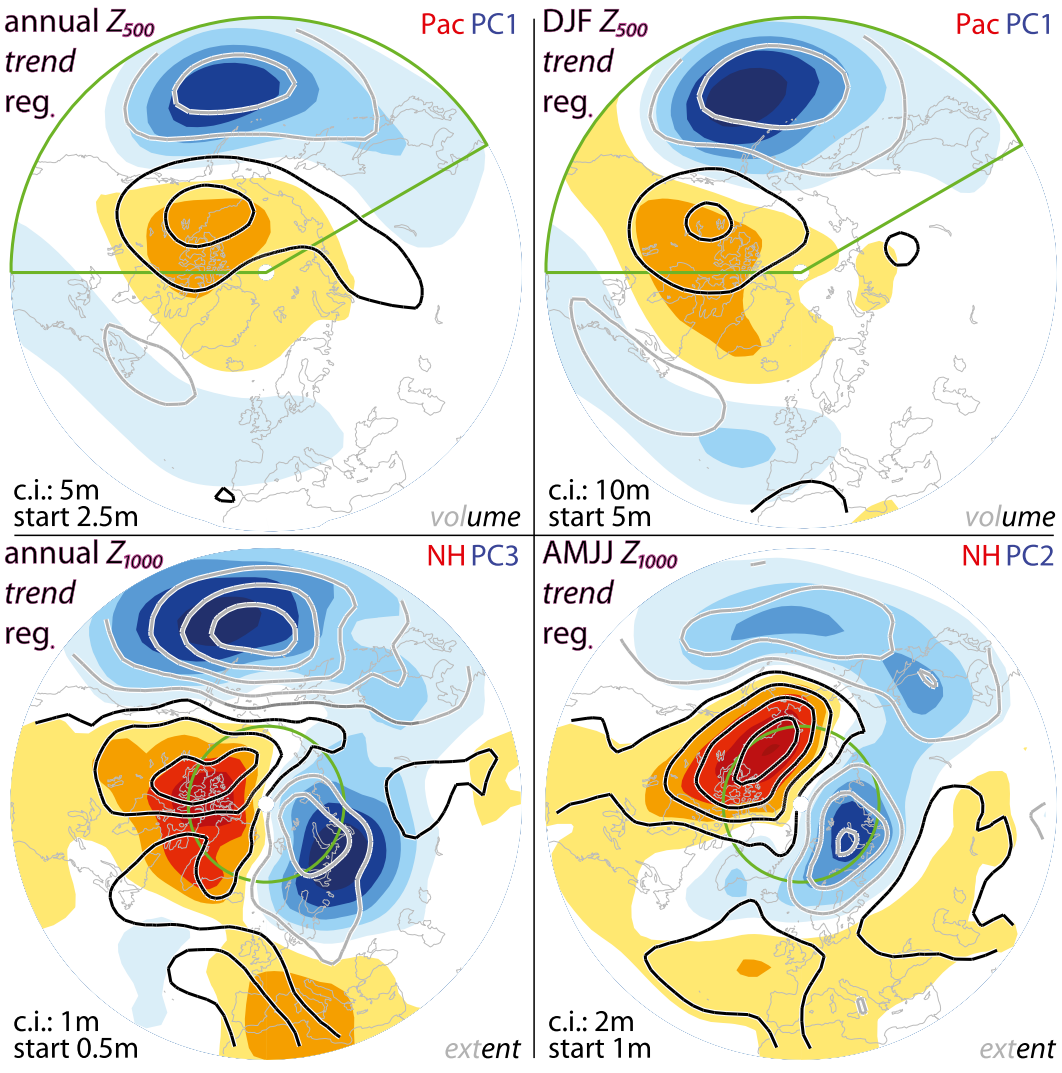


FIG. 10. Leading EOFs (color shading) of 2020–59 trends in (left) annual or (right) seasonal (top) $Z_{500}$ or (bottom) $Z_{1000}$ are calculated from the 39-member CCSM3 ensemble and displayed as regressions onto standardized values of the associated PCs. The $Z_{1000}$ and $Z_{500}$ EOFs are calculated for the AMJJ and DJF seasons during which the EXT associations with $Z_{1000}$ or the VOL associations with $Z_{500}$ are strongest (Figs. 5 and 6, respectively). The same annual or seasonal $Z_{500}$ and $Z_{1000}$ trends are also regressed (contours) onto the 39 CCSM3 VOL or EXT trend values as indicated. The $Z_{500}$ trend PCs are calculated poleward of 30°N in an extended Pacific sector (120°E–90°W) indicated by a green line. The $Z_{1000}$ trend PCs are calculated poleward of 70°N as indicated by the green circle. The contour interval for both maps in each panel is indicated in the lower left.

are accompanied by increased convective precipitation and latent heating over most of the tropical Pacific (not shown). The global structure of internal variability in atmospheric circulation trends associated with Arctic ice VOL can also be obtained from the leading PC of tropical Pacific $T_{ref}$ trends (right panels, Fig. 12). This pattern is reminiscent of a "global hyper mode" (Dommenget and Latif 2008) that may result from thermodynamic air–sea interaction (see also Clement et al. 2011).

The relevance of the tropical Pacific in internal Arctic sea ice loss variability is demonstrated more directly in Fig. 13, which provides maps comparable to those in Figs. 3a–c, but for annual ice and atmosphere trend regressions onto the first PC of tropical Pacific $T_{ref}$ trends instead of onto EXT trends. The regression maps show an Arctic dipole–like SLP pattern and associated near-surface winds (Fig. 13c) that drive a transpolar drift in ice velocity and ice advection out of the Arctic through the Fram Strait and into the Barents Sea (Fig. 13b). The

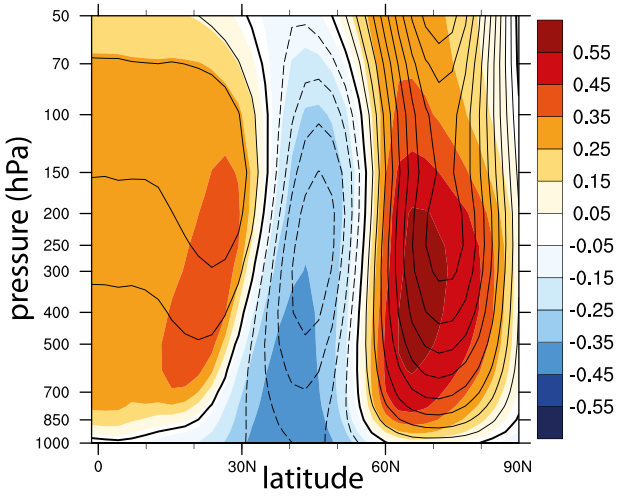


FIG. 11. Ensemble trend correlations (color shading) and ensemble trend regressions (contours) between annual (October–September) 2020–59 trends in the Pacific (120°E–90°W) zonal average geopotential height field and standardized 2020–59 JASON Arctic sea ice VOL trends. Thicker black contours represent a Pacific correlation/regression value of zero. Dashed contours indicate negative regression values. The regression contour interval is 1 m per standard deviation ($2.7 \times 10^3$ km$^3$) of the JASON VOL trends.

first PC of tropical Pacific $T_{ref}$ trends is also associated with negative sea ice concentration (Fig. 13a) and thickness (Fig. 13b) poleward of Alaska and Siberia.

## 4. Summary

This study's results can be summarized into the following key findings:

- Internal variability is an important factor influencing the magnitude and spatial pattern of twenty-first-century summer Arctic sea ice loss in the 39-member CCSM3 ensemble forced by the A1B GHG emissions scenario. Specifically, internal variability leads to a roughly threefold range in trends of ice EXT and VOL loss during 2020–59.
- This spread in the amount of ice loss is related to large-scale patterns of atmospheric circulation and accompanying ice motion fields.
  - In particular, an Arctic dipole–like pattern in SLP trends that is strongest in spring and early summer (April–July) is associated with Arctic sea ice advection across the central Arctic and export through the Fram Strait and into the Barents Sea.
  - Internal variability in sea ice loss trends is also associated with an atmospheric Rossby wave train pattern in the free troposphere, with centers of action over the North Pacific and downstream over northwestern North America and the western Atlantic. This Rossby wave train is emphasized during winter (December–February) but is present throughout the year.
- Each of these atmospheric pressure patterns is associated with a leading pattern of atmospheric trend variability within the ensemble, as determined through independent EOF/PC analysis.
- The atmospheric circulation patterns associated with internal variability in Arctic sea ice loss exhibit weak but significant teleconnections to the tropical and Southern Hemisphere Pacific in annual-mean data. Similar Pacific teleconnection patterns, with extensions over the Arctic, are associated with the leading PC of $T_{ref}$ trends over the tropical Pacific.
- Associations between sea ice and atmospheric circulation anomalies on interannual time scales are broadly similar to those that characterize the internal variability of 40-yr trends.
  - In particular, the spatial pattern and seasonal dependence of the atmospheric circulation anomalies that covary with high-pass filtered sea ice variability as well as the accompanying changes in trans-Arctic sea ice advection resemble those based on internal trend variability.
  - In CCSM3, high-pass filtered variability in Arctic sea ice loss is associated with ice advection through the Fram Strait and into the Barents Sea throughout the year preceding the summer Arctic sea ice minimum.
  - Interannual relationships between sea ice and atmospheric circulation anomalies simulated by CCSM3 are generally realistic except for a 30° rotation of the large-scale wind-driven ice motion across the central Arctic. This shortcoming is likely related to a bias in the CCSM3's climatological-mean sea ice thickness distribution, an aspect that is improved in CCSM4.

## 5. Discussion

The results of this study describe an important role for internal variability in twenty-first-century projections of Arctic sea ice loss and illustrate a consistent set of physically related patterns in the distribution of ice loss, ice motion, and atmospheric circulation variability. This discussion will elaborate on and provide an interpretation of some of the results.

Summer Arctic sea ice extent (Fig. 14a) and volume (Fig. 14b) projections from the smaller (e.g., 6–7 member) CCSM4 climate change ensembles (the same that were used to generate Figs. 9b,c) demonstrate that internal variability remains an important component of

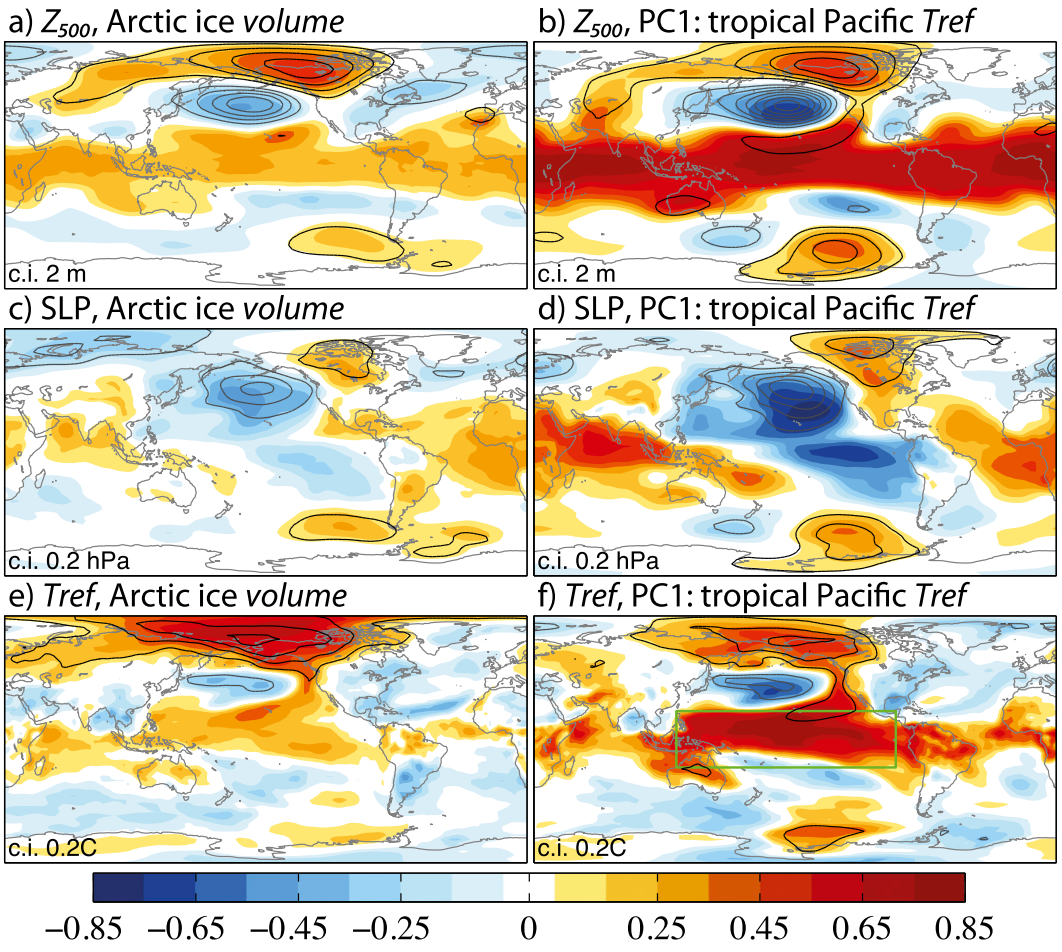


FIG. 12. Ensemble trend correlations (color shading) and ensemble trend regressions (contours) with (left) JASON VOL and with (right) the first PC of annual (October–September) tropical Pacific near-surface reference temperature ($T_{ref}$, PC1) are shown. Correlations with annual (October–September) 2020–59 trends in (a), (b) $Z_{500}$, (c),(d) SLP, and (e),(f) $T_{ref}$ indicate the global-scale atmospheric teleconnections with (left) Arctic ice loss and (right) tropical Pacific temperature. The tropical Pacific (20°S–20°N, 120°E–90°W) domain over which the $T_{ref}$ PCs were calculated is indicated by a green box in (f). Contour intervals for the regressions are indicated in the lower left of each panel.

uncertainty in the newest version of the model (see also Kay et al. 2011) as it is in the CCSM3 ensemble we analyzed. In particular, Fig. 14 suggests that internal variability will continue to be an important factor in future Arctic sea ice loss projections for at least the next several decades and that this conclusion is robust, not an artifact produced only within the CCSM3 ensemble. For instance, one CCSM4 ensemble member from the weakest equivalent GHG forcing scenario (RCP 2.6) is associated with the least extensive September sea ice as late as 2051, while a member from the second strongest equivalent GHG forcing scenario (RCP 6.0; similar to the SRES A1B) is associated with the most extensive September sea ice several times between 2052 and 2061. These two examples demonstrate the lingering influence of internal variability in CCSM4. A qualitative assessment of uncertainty in Arctic sea ice loss projections using other coupled models in the CMIP3 archive suggests that the three sources of uncertainty (magnitude of GHG forcing, model sensitivity, and internal variability) are all roughly comparable in the middle of the twenty-first century (not shown). This study describes an important role for internally generated variability in the magnitude of twenty-first-century Arctic sea ice loss; a generally similar result was obtained in a comparable but much smaller (5 member) coupled model ensemble (Sorteberg et al. 2005). Additional ensemble members with other fully coupled models are required for a more robust evaluation.

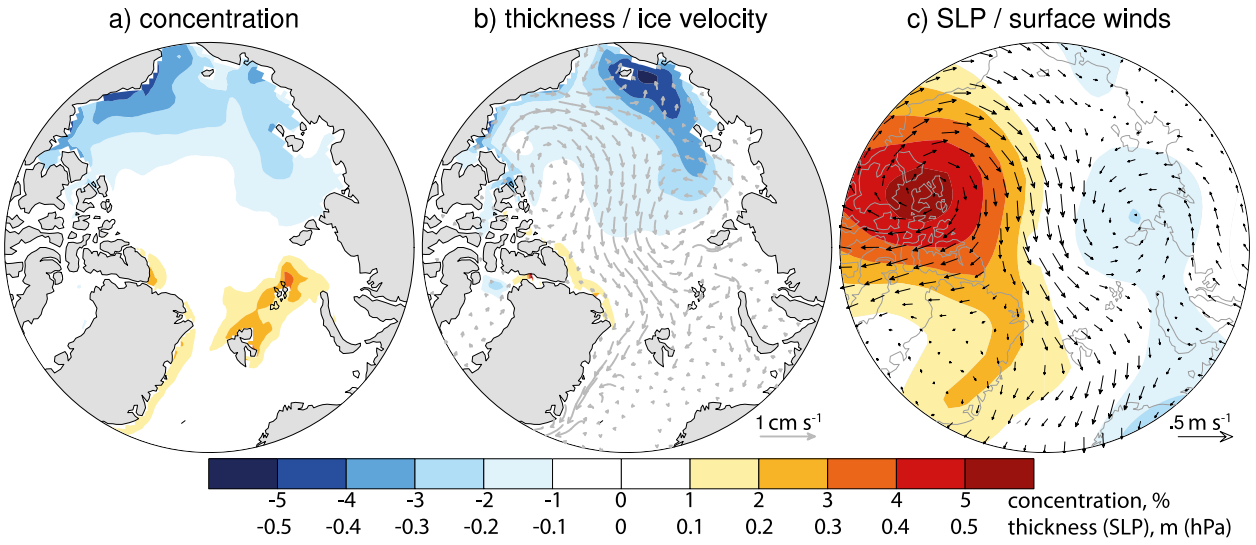


FIG. 13. As in the top panels of Fig. 3, but the trend regressions are onto the first PC of tropical Pacific near-surface temperature trends ($T_{ref}$ PC1) instead of onto Arctic EXT trends. See Fig. 12 and the text for more detail on the tropical Pacific $T_{ref}$ PC calculation.

The qualitative similarity of the results based on the internal variability of trends and that of the interannual variability suggests that similar atmospherically driven ice loss mechanisms operate over a broad range of time scales. Based on this similarity, we interpret the trend-based results as a natural consequence of large-scale atmospheric circulation variability that exists and apparently drives changes in Arctic sea ice cover over a broad range of time scales.

As alluded to in the introduction, distinguishing whether central Arctic atmospheric covariability with sea ice loss is more Arctic dipole (AD)–like or more Arctic Oscillation (AO)–like is an active area of research, but no clear consensus exists. Although the

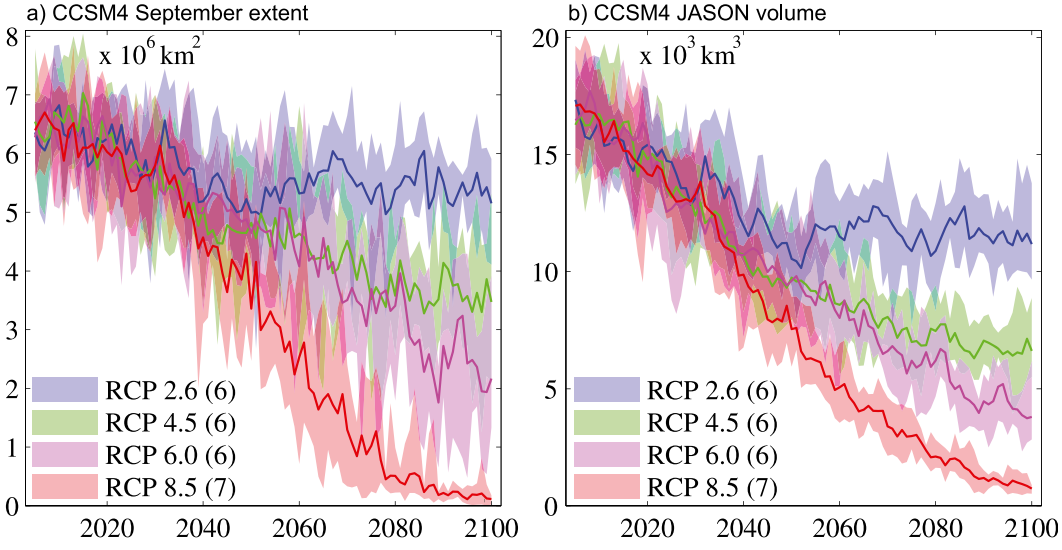


FIG. 14. Simulated twenty-first-century CCSM4 (a) September sea ice extent and (b) JASON sea ice volume are plotted as a function of CMIP5 RCP emissions scenarios indicated. The ensemble mean (thick solid lines) is shown along with the ensemble range (color shading) as represented by the minimum and maximum September sea ice extent or JASON sea ice volume value in each year for each RCP. The number of ensemble members is indicated in parenthesis next to the RCP scenario legend in the bottom left. The CCSM4 ensembles range from relatively weak equivalent GHG forcing (RCP2.6) to relatively strong equivalent GHG forcing (RCP8.5). More detail on the CCSM4 ensemble and the RCP scenarios is contained in the text.

analyses in this paper have emphasized an Arctic dipole–like pattern of atmospheric covariability, results have also documented generally stronger relationships with ice advection and corresponding surface winds than with any static pattern of atmospheric covariability (e.g., ensemble trend correlations with EXT are larger for surface winds than for SLP; see appendix, Fig. A1c). A similar conclusion has been distilled from the available observations (Smedsrud et al. 2011). In particular, our analysis of interannual time-scale variability (e.g., Fig. 7) and of intermediate time scales and composites of individual ice loss events (not shown) indicates that the patterns of surface pressure anomalies associated with ice loss evolve seasonally and can also change substantially from event to event, but that a transpolar drift in ice advection and Fram Strait/Barents Sea ice export are consistently involved. Note, for example, that the central Arctic $Z_{1000}$ regression pattern during June–July in Fig. 7 is associated with a negative AO-like pattern, but one whose polar center of action is concentrated over the Canadian Archipelago in the western Arctic that in turn affects surface winds throughout the Arctic basin. In general, the collection of results in this paper suggests a more flexible presumption about atmospheric covariability with ice loss is warranted. Insofar as the AD-like pattern is associated with atmospheric variability emanating from the tropical Pacific in a Rossby wave train (as it is in the CCSM3 ensemble), different flavors of both of the leading two patterns of extratropical surface pressure variability (the northern annular mode/AO and the PNA patterns) may in turn be associated with anomalous ice advection, ice export, and internal variability in sea ice loss. A pattern of SLP variability similar to the one we associate with internal variability in Arctic sea ice advection and export was linked to multidecadal climate variability in the Greenland Sea by Delworth et al. (1997).

Internal variability in CCSM3 Arctic sea ice loss is related mostly to internal variability in the North Pacific atmospheric circulation and has relatively little association with atmospheric circulation variability over the North Atlantic. The ensemble spread in atmospheric circulation trends over the North Pacific is distinct from the spatial pattern of the ensemble-mean (forced) trend over the North Pacific (not shown), so the covariability between Arctic sea ice loss and North Pacific atmospheric circulation has a clear association with natural variability. The similarity between Pacific atmospheric circulation covariability patterns with both Arctic ice VOL trends and the leading PC of tropical Pacific $T_{\mathrm{ref}}$ trend variability suggests that the tropical Pacific coherently influences subtropical, midlatitude, and even polar circulation variability in both hemispheres. The association between tropical Pacific variability and Arctic atmospheric circulation is consistent with ice removal from the central Arctic via ice export through the Fram Strait and into the Barents Sea.

Arctic sea ice loss in the CCSM3 ensemble is associated with the strength and longitudinal extent of the North Pacific subtropical jet (Fig. 3d) and with a Rossby wave train emanating from the subtropical Pacific (Figs. 4c and 6b). Both of these signatures have been associated with the PNA and a leading pattern of observed storm track–jet covariability in the North Pacific (Wettstein and Wallace 2010). The strength and longitudinal extent of the Pacific subtropical jet has also been related to variability in the intensity of tropical diabatic heating and the PNA (Li and Wettstein 2012). The mostly equivalent barotropic midlatitude structure, the similarity of Pacific teleconnections between Arctic sea ice loss and tropical Pacific $T_{\mathrm{ref}}$ variability, and the link to our understanding of midlatitude atmospheric dynamics all suggest that the internal variability we concentrate on in this paper is associated with an Arctic/downstream response to tropical Pacific variability rather than vice versa. Our results and interpretation are also broadly consistent with the influence of the tropical Pacific and a PNA-like pattern on Arctic surface air temperature described by Lee et al. (2011).

A few of the CCSM3-based interpretations discussed in the previous three paragraphs are worthy of special attention.

(i) A transpolar drift in ice advection and Fram Strait–Barents Sea ice export are consistently associated with internal variability in Arctic sea ice loss, even if the precise SLP patterns vary by event and time of year.
(ii) Internal variability in Arctic sea ice loss is related to internal variability in the large-scale atmospheric circulation not only over the Arctic, but also over the North Pacific (and not over the North Atlantic).
(iii) Internal variability of the Arctic and North Pacific atmospheric circulation is influenced by the tropical Pacific via Rossby wave dynamics. Thus, tropical Pacific variability may play a role in anomalous Arctic sea ice advection and export.

Both September ice EXT and July–November (JASON) ice VOL have been used in this study as indices of summer Arctic sea ice loss. Although the 40-yr trends of EXT and VOL are highly correlated across the 39-member ensemble ($r = 0.80$), roughly a third of the trend variance is unshared. Given that most of the trend variance is common between the two indices of summer Arctic sea ice loss, qualitatively similar patterns

and seasonality are obtained if an investigation of the seasonality of the Arctic dipole–like SLP association (e.g., Fig. 5) is based on VOL rather than EXT or if an investigation of the seasonality of the Rossby wave train association (e.g., Fig. 6) is based on EXT rather than VOL. That said, the particular pairing of SLP variability with EXT and $Z_{500}$ variability with VOL provides stronger, more consistent, and more physically intuitive patterns. Our interpretation of these results is that EXT is somewhat more sensitive to the AMJJ wind-driven ice advection, whereas VOL is responsive to a more integrated annual average of sea ice advection and export (e.g., Figs. 6 and 7). A related interpretation can be made for the roughly 30° counterclockwise pattern rotation of annually averaged atmospheric covariability with VOL relative to EXT (cf. Figs. 3c,e with Figs. 4b,c). Because VOL has a stronger relationship to annual sea ice advection and to the Pacific Rossby wave train, and also because the Pacific subtropical jet is stronger and zonally extended in winter (e.g., DJF) relative to late spring and early summer (e.g., AMJJ), the entire pattern of atmospheric covariability over the extratropical Pacific is shifted roughly 30° counterclockwise (downstream) in annual VOL regressions relative to annual EXT regressions. In general, the mechanism of ice advection and export we emphasize and associate with internal Arctic sea ice loss variability likely has a stronger and more coherent association with sea ice volume than with sea ice extent.

The large ensemble of twenty-first-century simulations by CCSM3 is currently a unique resource for exploring internal variability and its mechanisms, but there are some noteworthy caveats. As mentioned previously, the T42 resolution CCSM3 exhibits too much and improperly distributed Arctic sea ice relative to nature (DeWeaver and Bitz 2006). This bias could influence the simulated sensitivity to atmospheric forcing. In addition, like many CMIP3 models, CCSM3 generates El Niño–Southern Oscillation (ENSO) events that are too regular and too frequent, as well as a Pacific decadal oscillation (PDO) that lacks a strong connection between the tropics and the North Pacific. The extratropical atmospheric teleconnection patterns associated with both ENSO and PDO at their native simulated frequencies are nevertheless reasonable (Deser et al. 2006; Stoner et al. 2009).

By focusing on the sea ice response to atmospheric forcing, we largely neglect any feedbacks of the internal variability in ice loss trends upon the atmosphere. Previous studies have shown that the atmospheric circulation response to Arctic sea ice anomalies is generally much weaker than the atmospheric circulation patterns that force sea ice changes (see Magnusdottir et al. 2004; Deser et al. 2004; Kvamstø et al. 2004; Bhatt et al. 2008; Seierstad and Bader 2009; Deser et al. 2010; Serreze and Barry 2011; Blüthgen et al. 2012 and compare to references in the introduction). Preliminary results (not shown) indicate that the intensity of the SLP low over the eastern Arctic may be related to the atmospheric response to Arctic sea ice loss in the CCSM3 ensemble, broadly consistent with the findings of Blüthgen et al. (2012). Isolating the response and feedbacks to Arctic sea ice loss in the atmosphere, ocean, and sea ice in observations and in the fully coupled CCSM3 and CCSM4 ensembles is the subject of our ongoing research.

The results in this study are based on one model (CCSM3), with additional supporting evidence from CCSM4. Compared to CCSM3, CCSM4 shows an improved simulation of the distribution of Arctic sea ice (Jahn et al. 2012) and of the frequency spectrum of ENSO (Deser et al. 2012c), highlighting new opportunities for mechanistic studies using large ensembles as models become more realistic. Large ensembles of climate change simulations at a variety of resolutions with other models are needed to test the robustness of our findings based on CCSM, in particular both the central Arctic relationships and proposed associations with the midlatitude and tropical Pacific.

*Acknowledgments.* We thank Marika Holland, Alex Jahn, Jen Kay, Adam Phillips, and Dennis Shea, who have each contributed helpful suggestions on various aspects of this work. We would also like to thank John Walsh and two anonymous reviewers for their thoughtful comments. We made extensive use of the NCAR Command Language (NCL) and would like to acknowledge the National Science Foundation for their sponsorship of this effort and especially Dennis Shea for his support and guidance. J. W. was supported by a grant from the National Science Foundation Arctic Sciences Program.

## APPENDIX

### Annual Ensemble Spread Correlations with Extent

This paper has analyzed various features of internal variability in Arctic sea ice loss with a focus on atmospheric covariability. The annual ensemble trend regressions with EXT (Fig. 3) are probably the most general and comparable to other studies, but regression coefficients demonstrate the relationships only in physical units, whereas the amount of shared variance is also a useful quantity. Annual ensemble trend correlations

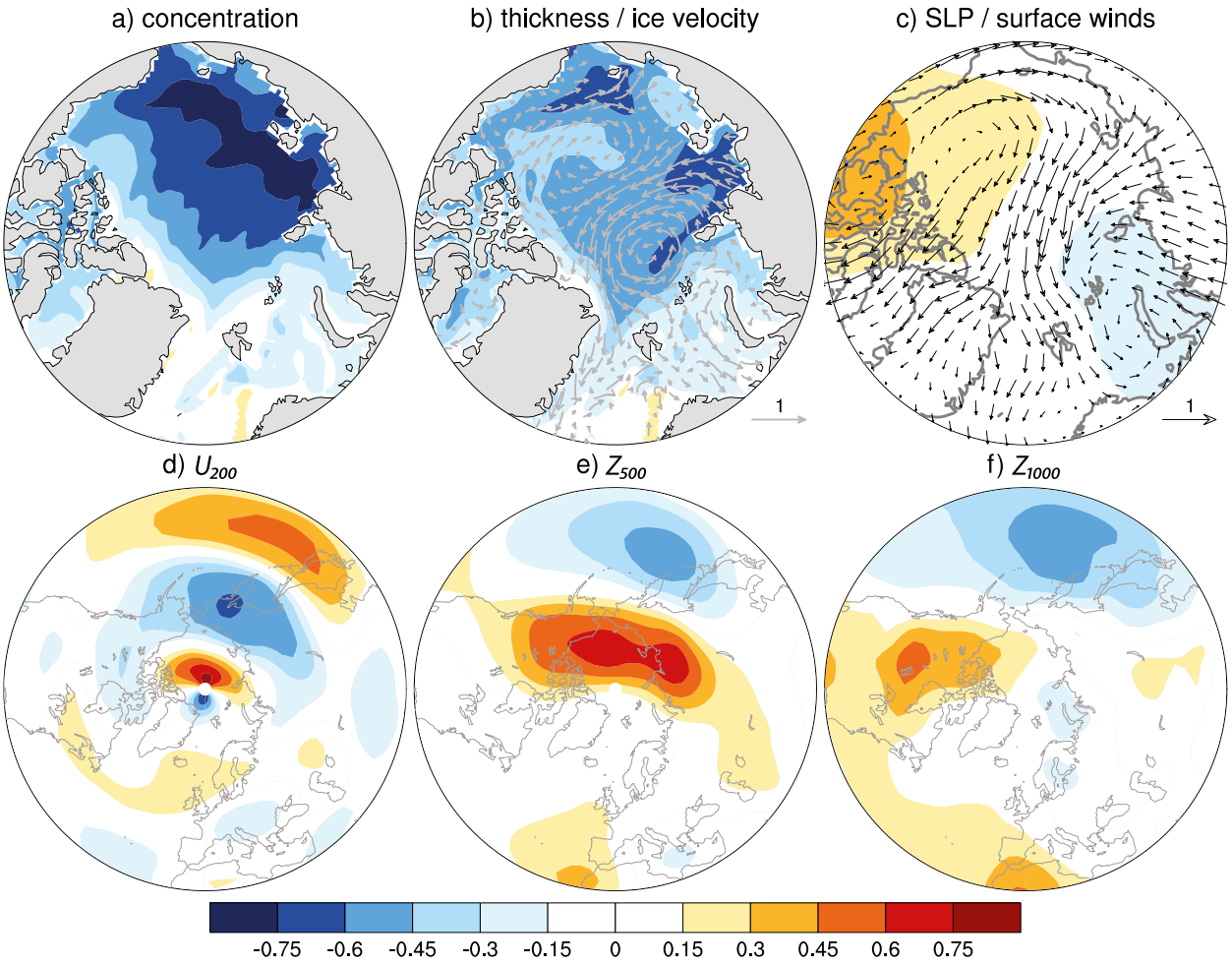


FIG. A1. As in Fig. 3, but ensemble trend correlations with EXT are shown instead of regressions.

with extent are shown in Fig. A1 for the same sea ice and atmospheric variables as in Fig. 3.

Ice concentration ensemble trend correlations with EXT are strongest in the Eurasian sector, diminish in magnitude across the central Arctic, and extend into a tongue within the Fram Strait (Fig. A1a). This distribution is roughly similar for ice thickness (Fig. A1b), but correlation magnitudes are lower because the index variable is EXT rather than VOL. The Arctic dipole–like ensemble trend correlation of SLP with EXT is weak, but stronger correlations exist with the SLP gradient (not shown) and with near-surface winds (Fig. A1c). A transpolar drift in ice velocity correlations is consistent with wind-driven ice export arguments elsewhere in this paper. Large-scale atmospheric covariability is also demonstrated by significant ensemble trend correlations outside the Arctic (Figs. A1d–f). Geopotential height correlations can be compared with those in Figs. 5, 6, 11, and 12.

## REFERENCES

Belchansky, G. I., D. C. Douglas, V. A. Eremeev, and N. G. Platonov, 2005: Variations in the Arctic's multiyear sea ice cover: A neural network analysis of SMMR-SSM/I data, 1979–2004. *Geophys. Res. Lett.,* **32,** L09605, doi:10.1029/2005GL022395.

Bhatt, U. S., M. A. Alexander, C. Deser, J. E. Walsh, J. S. Miller, M. S. Timlin, J. Scott, and R. A. Tomas, 2008: The atmospheric response to realistic reduced summer Arctic sea ice anomalies. *Arctic Sea Ice Decline: Observations, Projections, Mechanisms, and Implications, Geophys. Monogr.,* Vol. 180, Amer. Geophys. Union, 91–110.

Bitz, C. M., 2008: Some aspects of uncertainty in predicting sea ice thinning. *Arctic Sea Ice Decline: Observations, Projections, Mechanisms, and Implications, Geophys. Monogr.,* Vol. 180, Amer. Geophys. Union, 63–76.

——, J. K. Ridley, M. Holland, and H. Cattle, 2012: Global climate models and 20th and 21st century Arctic climate change. *Arctic Climate Change: The ACSYS Decade and Beyond,* P. Lemke and H.-W. Jacobi, Eds., Springer, 405–436.

Blüthgen, J., R. Gerdes, and M. Werner, 2012: Atmospheric response to the extreme Arctic sea ice conditions in 2007. *Geophys. Res. Lett.,* **39,** L02707, doi:10.1029/2011GL050486.

Boé, J., A. Hall, and X. Qu, 2010: Sources of spread in simulations of Arctic sea ice loss over the twenty-first century. *Climatic Change,* **99,** 637–645.

Branstator, G., and H. Teng, 2010: Two limits of initial-value decadal predictability in a CGCM. *J. Climate,* **23,** 6292–6311.

Clement, A., P. DiNezio, and C. Deser, 2011: Rethinking the ocean's role in the Southern Oscillation. *J. Climate,* **24,** 4056–4072.

Collins, W. D., and Coauthors, 2006: The Community Climate System Model version 3 (CCSM3). *J. Climate,* **19,** 2122–2143.

Comiso, J. C., C. L. Parkinson, R. Gersten, and L. Stock, 2008: Accelerated decline in the Arctic sea ice cover. *Geophys. Res. Lett.,* **35,** L01703, doi:10.1029/2007GL031972.

Delworth, T. L., S. Manabe, and R. J. Stouffer, 1997: Multidecadal climate variability in the Greenland Sea and surrounding regions: A coupled model simulation. *Geophys. Res. Lett.,* **24** (3), 257–260.

Deser, C., and H. Teng, 2008: Recent trends in Arctic sea ice and the evolving role of atmospheric circulation forcing, 1979–2007. *Arctic Sea Ice Decline: Observations, Projections, Mechanisms, and Implications, Geophys. Monogr.,* Vol. 180, Amer. Geophys. Union, 7–26.

——, G. Magnusdottir, R. Saravanan, and A. S. Phillips, 2004: The effects of North Atlantic SST and sea ice anomalies on the winter circulation in CCM3. Part II: Direct and indirect components of the response. *J. Climate,* **17,** 877–889.

——, A. Capotondi, R. Saravanan, and A. S. Phillips, 2006: Tropical Pacific and Atlantic climate variability in CCSM3. *J. Climate,* **19,** 2451–2481.

——, R. Tomas, M. Alexander, and D. Lawrence, 2010: The seasonal atmospheric response to projected Arctic sea ice loss in the late twenty-first century. *J. Climate,* **23,** 333–351.

——, R. Knutti, S. Solomon, and A. S. Phillips, 2012a: Communication of the role of natural variability in future North American climate. *Nat. Climate Change,* **2,** 775–779.

——, A. Phillips, V. Bourdette, and H. Teng, 2012b: Uncertainty in climate change projections: The role of internal variability. *Climate Dyn.,* **38,** 527–546.

——, and Coauthors, 2012c: ENSO and Pacific decadal variability in the Community Climate System Model version 4. *J. Climate,* **25,** 2622–2651.

DeWeaver, E., and C. M. Bitz, 2006: Atmospheric circulation and its effect on Arctic sea ice in CCSM3 simulations at medium and high resolution. *J. Climate,* **19,** 2415–2436.

——, E. C. Hunke, and M. M. Holland, 2008: Sensitivity of Arctic sea ice thickness to intermodel variations in the surface energy budget. *Arctic Sea Ice Decline: Observations, Projections, Mechanisms, and Implications, Geophys. Monogr.,* Vol. 180, Amer. Geophys. Union, 77–90.

Dommenget, D., and M. Latif, 2008: Generation of hyper climate modes. *Geophys. Res. Lett.,* **35,** L02706, doi:10.1029/2007GL031087.

Fetterer, F., K. Knowles, W. Meier, and M. Savoie, 2002: Sea ice index. National Snow and Ice Data Center, Boulder, CO, digital media. [Available online at http://nsidc.org/data/g02135.html.]

Fowler, C., 2003: Polar Pathfinder daily 25 km EASE-grid sea ice motion vectors. National Snow and Ice Data Center, Boulder, CO, digital media. [Available online at http://nsidc.org/data/docs/daac/nsidc0116_icemotion.gd.html.]

Francis, J. A., and E. Hunter, 2007: Drivers of declining sea ice in the Arctic winter: A tale of two seas. *Geophys. Res. Lett.,* **34,** L17503, doi:10.1029/2007GL030995.

Gent, P. R., and Coauthors, 2011: The Community Climate System Model version 4. *J. Climate,* **24,** 4973–4991.

Hawkins, E., and R. Sutton, 2009: The potential to narrow uncertainty in regional climate predictions. *Bull. Amer. Meteor. Soc.,* **90,** 1095–1107.

Holland, M. M., and C. M. Bitz, 2003: Polar amplification of climate change in coupled models. *Climate Dyn.,* **21,** 221–232.

——, ——, L.-B. Tremblay, and D. A. Bailey, 2008: The role of natural versus forced change in future rapid summer Arctic ice loss. *Arctic Sea Ice Decline: Observations, Projections, Mechanisms, and Implications, Geophys. Monogr.,* Vol. 180, Amer. Geophys. Union, 133–150.

Hu, Z.-Z., A. Kumar, B. Jha, and B. Huang, 2012: An analysis of forced and internal variability in a warmer climate in CCSM3. *J. Climate,* **25,** 2356–2373.

Jahn, A., and Coauthors, 2012: Late-twentieth-century simulation of Arctic sea ice and ocean properties in the CCSM4. *J. Climate,* **25,** 1431–1452.

Kay, J. E., M. M. Holland, and A. Jahn, 2011: Inter-annual to multi-decadal Arctic sea ice extent trends in a warming world. *Geophys. Res. Lett.,* **38,** L15708, doi:10.1029/2011GL048008.

——, ——, C. M. Bitz, E. Blanchard-Wrigglesworth, A. Gettelman, A. Conley, and D. Bailey, 2012: The influence of local feedbacks and northward heat transport on the equilibrium Arctic climate response to increased greenhouse gas forcing. *J. Climate,* **25,** 5433–5450.

Kvamstø, N. G., P. Skeie, and D. B. Stephenson, 2004: Impact of Labrador sea-ice extent on the North Atlantic Oscillation. *Int. J. Climatol.,* **24,** 603–612.

Lee, S., T. Gong, N. Johnson, S. B. Feldstein, and D. Pollard, 2011: On the possible link between tropical convection and the Northern Hemisphere Arctic surface air temperature change between 1958 and 2001. *J. Climate,* **24,** 4350–4367.

L'Heureux, M. L., A. Kumar, G. D. Bell, M. S. Halpert, and R. W. Higgins, 2008: Role of the Pacific-North American (PNA) pattern in the 2007 Arctic sea ice decline. *Geophys. Res. Lett.,* **35,** L20701, doi:10.1029/2008GL035205.

Li, C., and J. J. Wettstein, 2012: Thermally driven and eddy-driven jet variability in reanalysis. *J. Climate,* **25,** 1587–1596.

Magnusdottir, G., C. Deser, and R. Saravanan, 2004: The effects of North Atlantic SST and sea ice anomalies on the winter circulation in CCM3. Part I: Main features and storm-track characteristics of the response. *J. Climate,* **17,** 857–876.

Mahlstein, I., and R. Knutti, 2011: Ocean heat transport as a cause for model uncertainty in projected Arctic warming. *J. Climate,* **24,** 1451–1460.

Maslanik, J. A., C. Fowler, J. Stroeve, S. Drobot, H. J. Zwally, D. Yi, and W. J. Emery, 2007: A younger, thinner ice cover: Increased potential for rapid, extensive sea-ice loss. *Geophys. Res. Lett.,* **34,** L24501, doi:10.1029/2007GL032043.

Meehl, G. A., and Coauthors, 2006: Climate change projections for the twenty-first century and climate change commitment in the CCSM3. *J. Climate,* **19,** 2597–2616.

——, and Coauthors, 2012: Climate system response to external forcings and climate change projections in CCSM4. *J. Climate,* **25,** 3661–3683.

Moss, R. H., and Coauthors, 2010: The next generation of scenarios for climate change research and assessment. *Nature,* **463,** 747–756.

Nghiem, S. V., Y. Chao, G. Neumann, P. Li, D. K. Perovich, T. Street, and P. Clemente-Colon, 2006: Depletion of perennial sea ice in the east Arctic Ocean. *Geophys. Res. Lett.,* **33,** L17501, doi:10.1029/2006GL027198.

North, G. R., T. L. Bell, R. F. Cahalan, and F. J. Moeng, 1982: Sampling errors in the estimation of empirical orthogonal functions. *Mon. Wea. Rev.,* **110,** 699–706.

Ogi, M., and J. M. Wallace, 2007: Summer minimum Arctic sea ice extent and the associated summer atmospheric circulation. *Geophys. Res. Lett.,* **34,** L12705, doi:10.1029/2007GL029897.

——, and ——, 2012: The role of summer surface wind anomalies in the summer Arctic sea ice extent in 2010 and 2011. *Geophys. Res. Lett.,* **39,** L09704, doi:10.1029/2012GL051330.

——, K. Yamazaki, and J. M. Wallace, 2010: Influence of winter and summer surface wind anomalies on summer Arctic sea ice extent. *Geophys. Res. Lett.,* **37,** L07701, doi:10.1029/2009GL042356.

Overland, J. E., and M. Wang, 2005: The third Arctic climate pattern: 1930s and early 2000s. *Geophys. Res. Lett.,* **32,** L23808, doi:10.1029/2005GL024254.

——, and ——, 2010: Large-scale atmospheric circulation changes are associated with the recent loss of Arctic sea ice. *Tellus,* **62A,** 1–9.

Perovich, D. K., B. Light, H. Eicken, K. F. Jones, K. Runciman, and S. V. Nghiem, 2007: Increasing solar heating of the Arctic Ocean and adjacent seas, 1979–2005: Attribution and role in the ice-albedo feedback. *Geophys. Res. Lett.,* **34,** L19505, doi:10.1029/2007GL031480.

Polyakov, I. V., and Coauthors, 2005: One more step toward a warmer Arctic. *Geophys. Res. Lett.,* **32,** L17605, doi:10.1029/2005GL023740.

Rigor, I. G., and J. M. Wallace, 2004: Variations in the age of Arctic sea-ice and summer sea ice extent. *Geophys. Res. Lett.,* **31,** L09401, doi:10.1029/2004GL019492.

——, ——, and R. L. Colony, 2002: Response of sea ice to the Arctic Oscillation. *J. Climate,* **15,** 2648–2663.

Rothrock, D. A., Y. Yu, and G. A. Maykut, 1999: Thinning of the Arctic sea-ice cover. *Geophys. Res. Lett.,* **26** (23), 3469–3472.

Screen, J. A., I. Simmonds, and K. Keay, 2011: Dramatic interannual changes of perennial Arctic sea ice linked to abnormal summer storm activity. *J. Geophys. Res.,* **116,** D15105, doi:10.1029/2011JD015847.

Seierstad, I. A., and J. Bader, 2009: Impact of a projected future Arctic sea ice reduction on extratropical storminess and the NAO. *Climate Dyn.,* **33,** 937–943, doi:10.1007/s00382-008-0463-x.

Serreze, M. C., and R. G. Barry, 2011: Processes and impacts of Arctic amplification: A research synthesis. *Global Planet. Change,* **77,** 85–96.

——, M. M. Holland, and J. Stroeve, 2007: Perspectives on the Arctic's shrinking sea-ice cover. *Science,* **315,** 1533–1536.

Shimada, K., T. Kamoshida, M. Itoh, S. Nishio, E. Carmack, F. McLaughlin, S. Zimmerman, and A. Proshutinsky, 2006: Pacific Ocean inflow: Influence on catastrophic reduction of sea ice cover in the Arctic Ocean. *Geophys. Res. Lett.,* **33,** L08605, doi:10.1029/2005GL025624.

Simmons, A., S. Uppala, D. P. Dee, and S. Kobayashi, 2007: ERA-Interim: New ECMWF reanalysis products from 1989 onwards. *ECMWF Newsletter,* No. 110, ECMWF, Reading, United Kingdom, 25–35.

Smedsrud, L. H., A. Sirevaag, K. Kloster, A. Sorteberg, and S. Sandven, 2011: Recent wind driven high sea ice area export in the Fram Strait contributes to Arctic sea ice decline. *Cryosphere,* **5,** 821–829.

Sorteberg, A., T. Furevik, H. Drange, and N. G. Kvamstø, 2005: Effects of simulated natural variability on Arctic temperature projections. *Geophys. Res. Lett.,* **32,** L18708, doi:10.1029/2005GL023404.

Stoner, A. M. K., K. Hayhoe, and D. J. Wuebbles, 2009: Assessing general circulation model simulations of atmospheric teleconnection patterns. *J. Climate,* **22,** 4348–4372.

Stroeve, J. C., M. W. Holland, W. Meier, T. Scambos, and M. Serreze, 2007: Arctic sea ice decline: Faster than forecast. *Geophys. Res. Lett.,* **34,** L09501, doi:10.1029/2007GL029703.

——, J. Maslanik, M. C. Serreze, I. Rigor, W. Meier, and C. Fowler, 2011: Sea ice response to an extreme negative phase of the Arctic Oscillation during winter 2009/2010. *Geophys. Res. Lett.,* **38,** L02502, doi:10.1029/2010GL045662.

——, V. Kattsov, A. Barrett, M. Serreze, T. Pavlova, M. Holland, and W. N. Meier, 2012: Trends in Arctic sea ice extent from CMIP5, CMIP3 and observations. *Geophys. Res. Lett.,* **39,** L16502, doi:10.1029/2012GL052676.

Tebaldi, C., and R. Knutti, 2007: The use of the multimodel ensemble in probabilistic climate projections. *Philos. Trans. Roy. Soc. London,* **A365,** 2053–2075.

Teng, H., and G. Branstator, 2011: Initial-value predictability of prominent modes of North Pacific subsurface temperature in a CGCM. *Climate Dyn.,* **36,** 1813–1834, doi:10.1007/s00382-010-0749-7.

Thompson, D. W. J., and J. M. Wallace, 1998: The Arctic Oscillation signature in the wintertime geopotential height and temperature fields. *Geophys. Res. Lett.,* **25** (9), 1297–1300.

Tsukernik, M., C. Deser, M. Alexander, and R. Tomas, 2010: Atmospheric forcing of Fram Strait sea ice export: A closer look. *Climate Dyn.,* **35,** 1349–1360, doi:10.1007/s00382-009-0647-z.

Vavrus, S. J., M. M. Holland, A. Jahn, D. A. Bailey, and B. A. Blazey, 2012: Twenty-first-century Arctic climate change in CCSM4. *J. Climate,* **25,** 2696–2710.

Vinje, T., 2001: Fram Strait ice fluxes and atmospheric circulation: 1950–2000. *J. Climate,* **14,** 3508–3517.

Wang, J., J. Zhang, E. Watanabe, M. Ikeda, K. Mizobata, J. E. Walsh, X. Bai, and B. Wu, 2009: Is the dipole anomaly a major driver to record lows in Arctic summer sea ice extent? *Geophys. Res. Lett.,* **36,** L05706, doi:10.1029/2008GL036706.

Wettstein, J. J., and J. M. Wallace, 2010: Observed patterns of month-to-month storm-track variability and their relationship to the background flow. *J. Atmos. Sci.,* **67,** 1420–1437.

Winton, M., 2008: Sea ice-albedo feedback and nonlinear Arctic climate change. *Arctic Sea Ice Decline: Observations, Projections, Mechanisms, and Implications, Geophys. Monogr.,* Vol. 180, Amer. Geophys. Union, 111–131.

Wu, B., J. Wang, and J. E. Walsh, 2006: Dipole anomaly in the winter Arctic atmosphere and its association with sea ice motion. *J. Climate,* **19,** 210–225.